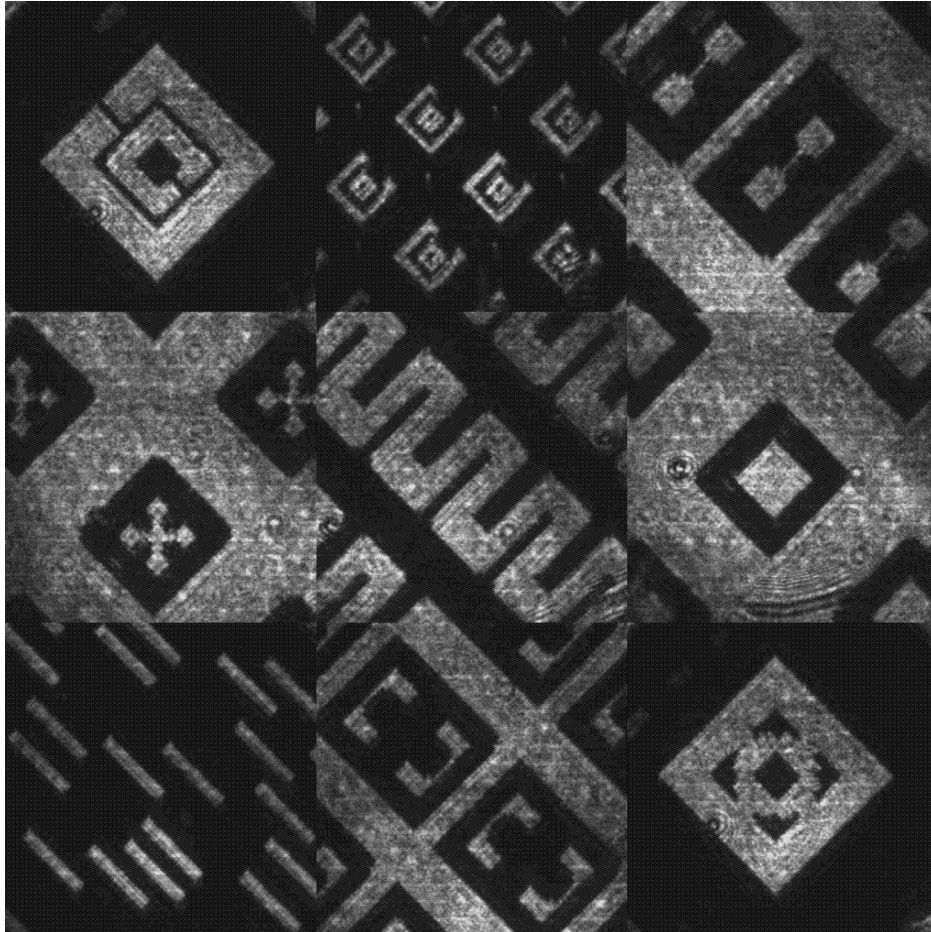


A 2D Spatial Light Modulator for femtosecond THz light modulation

Master Thesis

by Patrick Müller



Submitted: 25.03.2017

Primary supervisor: Prof. Dr. Ulrike Woggon (Technical University Berlin)

Secondary supervisor: Prof. Dr. Martin Wolf (Fritz-Haber-Institute of the Max-Planck-Society)



The figure on the cover page shows a collection of various metamaterial shapes, which are imprinted onto the intensity cross-section of fs-laser pulse by a spatial light modulator. The intensity profile is recorded with a charge-coupled device camera.

Contents

1. Introduction	1
1.1. Electromagnetic spectrum and THz frequencies	1
1.2. Light management/control by metamaterials	3
1.3. This thesis	3
2. Theoretical background	7
2.1. Metamaterials	7
2.1.1. Effective medium theory	8
2.1.2. Complementary metamaterials and Babinet's principle	9
2.2. Patterned photo-excitation	12
2.2.1. Spatial light modulator	12
2.2.2. Properties of photo-excited semiconductors	14
3. Experimental details	17
3.1. Laser system	17
3.2. Imaging setup	19
3.3. Terahertz generation and detection	24
4. Results and discussion	27
4.1. Unexcited sample optical constants	28
4.2. Photo-excitation	30
4.3. Wire grid THz polarizer	34
4.4. THz dipole antennas	41
4.5. Outlook: Metamaterial for local field enhancement	44
A. Appendix	51
A.1. SLM phase shift calibration - Contrast	51
A.2. Fresnel transmission formulae	53
A.3. Pump-pulse absorption pattern	55
A.4. Windowing effects on Fourier transformation	57
A.5. 2D cross correlation - global image quality	59
Bibliography	61

1. Introduction

1.1. Electromagnetic spectrum and THz frequencies

The terahertz (THz) spectral range roughly covering frequencies from 0.1 to 50 THz is a highly interesting spectral region. In the 1970s, the field of terahertz spectroscopy gained popularity [Fle74, Sie02] through its usefulness in probing numerous low-energy excitations, e.g. electronic band structure or lattice vibrations in solids, charge carrier dynamics in fluids or vibrational and rotational degrees of freedoms of molecules in gases [Sha99, Kam13]. In modern science, THz radiation is utilized for the examination several low-energy excitations as shown in figure 1.1. In solid state physics, magnons [Kam10], cooper pairs in high-temperature semiconductors [Sax12], ionization energies of excitons in semiconductors [Lei08], phonons [Mau04] or polaritons [Feu03] can be excitation with terahertz radiation. Likewise in gases and fluids, several rotational and stretching modes of molecules have their resonances in the THz regime [Did07]. In addition, scale-model experimentation with THz radiation allows for studying the behavior of longer wavelengths, e.g. propagation in random media [Jia03].

Regarding application-oriented science, higher operation speed, especially in the wireless telecommunication, is aspired. Devices, such as wireless local area networks (WLAN) [Fed10], fiber telecommunication schemes [Hil11] and FETs [dA11] are gradually approaching bandwidths on the THz scale to fulfill those needs. Furthermore, the low-energy and therefore non-destructive character of THz radiation is beneficial for in vivo applications in biology and imaging in medicine [Sie04], security [Kaw03] and body scans [Lew06]. Lately, the enhanced detection of microorganisms [Par14] and sugar [Lee15] using terahertz metamaterials was shown.

A natural source of terahertz radiation is black-body radiation with temperatures higher than 10 K. While this thermal emission is faint, it is crucial for astronomical observations in the interstellar medium [Tha13]. Advanced techniques in optical rectification and photoconduction [Aus83, Smi88] allowed access to terahertz radiation through multimode lasers [Can81, vE89], such as Ti:sapphire based lasers and FELs. Van Exter et al. introduced terahertz time-domain spectroscopy (THz-TDS), which allowed for the extraction of complex material parameters.

1. Introduction

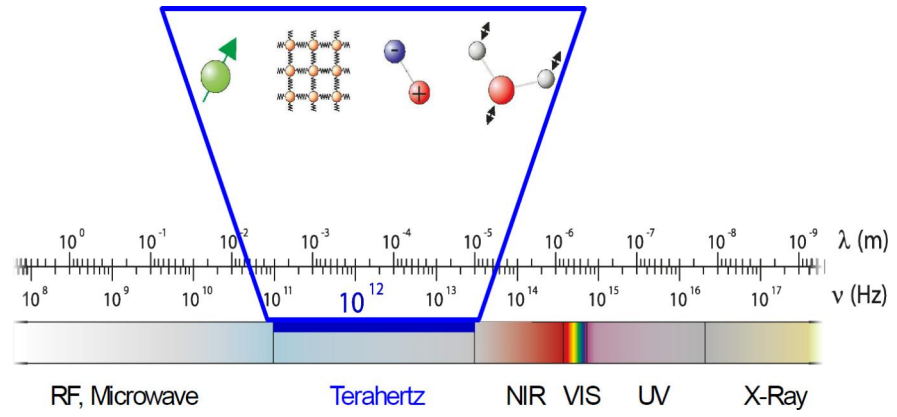


Figure 1.1.: The terahertz regime covers the frequency domain of 0.1 to 50 THz, corresponding to wavelengths from 6 to 3000 μm . It lies inbetween the microwave and near infrared regions (NIR). Shown in the inset are various low-energy excitations such as spin excitations, lattice vibrations, excitons in solids or vibrational modes of molecules.

1.2. Light management/control by metamaterials

Terahertz radiation occupies an intermediate position in the electromagnetic spectrum, filling the gap between infrared and microwave radiation. Conventional optics made from glass are useless for THz applications because of excessive extrinsic losses from charged defects [Naf07]. On the other hand some materials, including polymers, dielectrics and semiconductors are highly transmissive. Especially polymers, such as Teflon (PTFE) or polyethylene (PE) are transparent and almost dispersion free [Pod08] at low THz frequencies and used as windows and lenses [Sch11], but lose their transparency at higher frequencies. Metal surfaces or coated mirrors are commonly used as reflectors or when parabolic shaped as focusing, steering and collimating devices [Pei13].

In contrast to these established optics, polarization optics are difficult to realize with natural materials. Instead periodic artificial subwavelength structures ($a < \frac{\lambda}{10}$), so called, metamaterials have been introduced [Pen99], whose properties are not mainly based on constituent atoms, but designed structure. Metamaterials can be utilized as wire grid polarizers [Yam09], waveplates [Yu12, Che09] or frequency filters [Yen04, O'H07]. The manufacturing process, typically lithography [Mos05] or deposition [Tao08], however is exigent and the outcome is a static, binary element.

Although basic control over THz radiation can be established with passive optical elements, traditional metamaterials typically offer only narrow bandwidths. Bingham et al. combined various types of unit cells, superimposing their resonances [Bin08] for broadband properties. While these metamaterial groups enable exact tailoring of the optical properties, they remain static. Nonetheless dynamic elements like modulators, switches and frequency shifters are needed for short-range wireless THz communication or ultrafast THz interconnects, but cannot be realized with the previous lithography or deposition processes.

There are several proposals for active/tunable metamaterials [Zhe16], which can control transmission and reflection of the source radiation. These involve direct structural change to the unit cells by varying capacitance or conductance [Gil04], through nanomechanical actuators [Zhu11], using chemically [Pry10], thermally [Sin11, Che06], electrically [Zha07], magnetically [Hau08] or optically [Che08b] sensitive materials to change material properties. These active metamaterials achieve high transmission and reflection tunability, but small spectral tunability and are extremely demanding in processing.

1.3. This thesis

In this thesis, we conversely present an all-optical approach for versatile and selective active metamaterials in the THz regime. Illuminating a semiconductor with photons of energies, exceeding that of the bandgap, induces electron-hole pairs that contribute to the conduction of electrical charge. When projecting an intensity distribution, i.e. a gray scale image, on the semiconductor, this mask will be converted into a spatially varying density of charge carriers in the semiconductor, inducing a refractive-index landscape as shown in Figure 1.2. A spatial light modulator (SLM), a liquid

1. Introduction

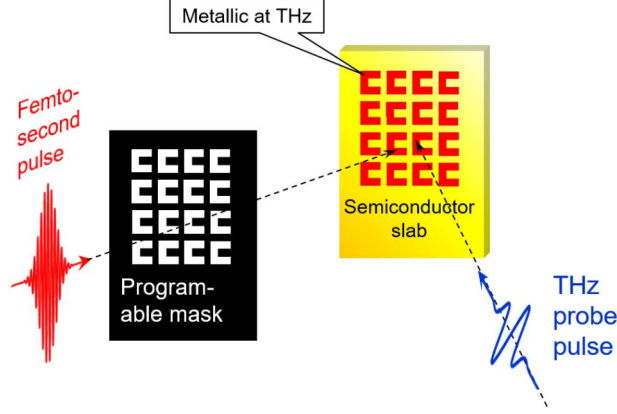


Figure 1.2.: A programmable mask shapes the spatial intensity profile of an infrared fs pump pulse, which is incident on a semiconductor slab. According to the Drude model, a local photo-excitation leads to a decrease of the local refractive index, therefore creating a transient refractive index landscape. When shaped corresponding to the effective medium theory, the subwavelength landscape can modulate a propagating THz probe similar to a metamaterial. The modulation lasts, while the excitation remains, but decays after a short time (roughly ps to ns), allowing transient control over the propagating THz radiation.

crystal display, enables reconfigurable spatial light shaping. Photo-generated metamaterials have been theoretically proposed by Rizza et al. [Riz13] and photo-generated THz wire grid polarizers on Si have been recently demonstrated by Kamaraju and coworkers by illumination through a printed mask [Kam14]. Georgiou et al. [Geo14] demonstrated all-optical generation of dipole antennas at THz frequencies. Photo-generated THz diffraction gratings by a spatial light modulator was established by Okada [Oka10, Oka11]. Busch and Xie [Bus12, Xie13] achieved THz beam steering using photoactive diffraction gratings.

While offering great flexibility regarding structure shaping, photo-generated metamaterials pose challenges in realization. The quality of the transient metamaterial depends crucially on aberration-free imaging. Furthermore the efficiency of THz modulation requires high dielectric contrast between illuminated and dark areas. Therefore, a superior modulation depth of the SLM is necessary. At the same time, disturbances in the SLM operation like phase fluctuations, voltage crosstalk and surface curvature of the LCD [Rei13, Kac06] have to be compensated or minimized through various calibration/modulation techniques.

To accomplish this goal, THz-TDS probes the semiconductor comparing an unexcited reference and induced dielectric properties under varying pump-patterns and -intensities. Generated through optical rectification in a Zinc telluride (ZnTe) crystal, THz radiation passes through a semiconductor is measured in a electro optic sampling (EOS) setup allowing precise mapping of the electric field and phase in the time domain.

By using photo-induced free charge carriers in semiconductors, transient metamaterials offer a unique method to dynamically and flexibly control terahertz radiation. A liquid crystal technique is presented, which allows fast (300 Hz) and precise probe-pulse modulation.

To evaluate the modulation of the transient structures in semiconductors, the transmitted THz transient is measured and compared to the unexcited transmission. With this technique the complex optical properties, e.g. phase, can be extracted. Fitting the Drude model to homogeneously

excited samples gives information about the free charge carrier generation and therefore complex refractive index. The fluence dependency of the complex refractive index is used to validate the Babinet's principle for transient wire-grid polarizers, which are studied regarding size, fluence and polarization variations. A dynamically generated transient wire grid polarizer is presented, which competes with current static mask induced polarizers. Furthermore, transient THz antennas are established, enabling broadband filtering. Utilizing a rectangular ring pattern, the induced carrier distribution shows resonance behavior in the low frequency THz regime. The thesis is concluded with an outlook towards narrow band-stop filter metamaterials, which are promising for future applications.

2. Theoretical background

This chapter briefly reviews the concept and fundamental theory for transient THz modulation. Illuminating a semiconductor layer with photons exceeding the bandgap energy generates electron-hole pairs that, according to the Drude model, contribute to the conduction of electrical charge. When projecting an image on the semiconductor, this image will be converted into a spatial charge carrier distribution in the semiconductor, which is proportional to the pump power. For a ns time frame, the induced charge carriers are confined to these illuminated areas, and the projected image is translated into a local permittivity modulation, as shown in figure 1.2. Based on the effective medium approximation, the incoming THz radiation cannot distinguish between the individual permittivity variations, but instead receives an effective response, which is governed by the geometry of confined charge carriers. In the following, the generation of programmable masks for selective photo-excitation and thus induced electron conductivity inside the semiconductor is explained. The effective medium approximation and relation between metamaterials and complementary structures according to Babinet's principle is reviewed.

2.1. Metamaterials

Metamaterials are composite structures, typically consisting of conductive metal and dielectric substrate, that are engineered to modify the electromagnetic properties of materials. The dimensions of a unit cell are smaller than the operation wavelength ($\sim \lambda_0/10$), so they can be operated in the quasi-static limit [Pen99, Cai10]. In this fashion, incoming radiation cannot distinguish the individual components. As can be seen in figure 2.1, the local \mathbf{E} field distribution over a unit cell varies slowly so the excitation can be approximated as an uniform field. Derived from the effective medium approximation, the total properties can then be described by the macroscopic qualities, such as electrical permittivity (ε) and magnetic permeability (μ). The properties of metamaterials are mainly controlled by their geometry but less by the intrinsic properties of the materials, offering scalability. As Maxwell's equations are scale invariance, the geometric effect at one frequency can be reproduced to the other by scaling their dimensions accordingly. Especially in the low THz regime, wavelengths are around hundreds of micrometers, making unit cells more practical compared to the optical regime.

2. Theoretical background

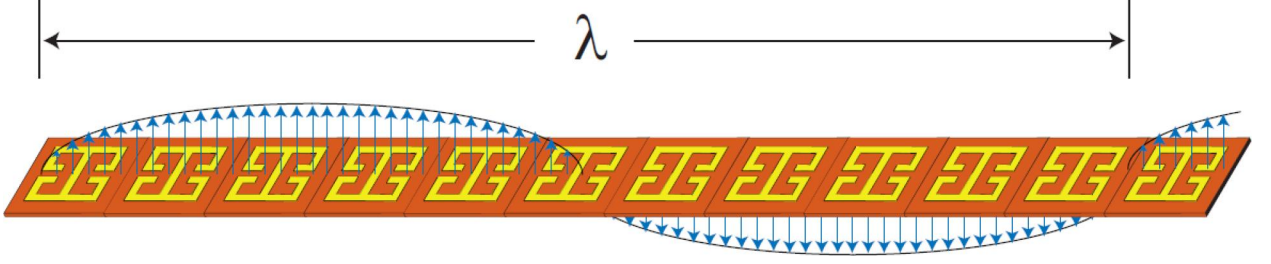


Figure 2.1.: Light propagating through a 1D metamaterial array in the long wavelength limit $\lambda \gg a$ is not sensitive to the microscopic detail, but to the macroscopic response. Metamaterials can thus be treated as homogeneous media, which are governed by geometry but less by intrinsic properties.

2.1.1. Effective medium theory

Various effective medium approaches like the Maxwell-Garnett or Clausius-Mossotti approximation were used to determine the dielectric constant of periodic composite materials. The long-wavelength limit is a very important case for which some analytical general results are available from theories known as effective medium theory or mean-field theory in the literature. One important result is the genuine equivalence between periodic artificial media and homogeneous material. For instance, 1D periodic structures are equivalent to uniaxial crystals with form birefringence [Bor70]. For these structures, the effective permittivity for a plane wave being normally incident to the surface and polarized in the x - y plane, the parallel and orthogonal polarized are given respectively by

$$\varepsilon_{||} = \frac{1}{\Lambda} \int \varepsilon(x) dx \quad \text{and} \quad \varepsilon_{\perp} = \frac{1}{\Lambda} \int \frac{1}{\varepsilon(x)} dx \quad (2.1)$$

where Λ denotes the period, ε the relative dielectric permittivity of the periodic structures and the integral describes spatial averaging. 2D and 3D periodic structures are in general equivalent to biaxial crystals, but, with few exceptions, no closed-form expressions exist.

Example effective medium: wire grid polarizer

A common example for metamaterials are wire grid polarizers (WGP). WGPs have been studied extensively as subwavelength structures consisting of periodically aligned wires, which reflect polarization of incident wave parallel to the wires while transmitting perpendicular polarization. The electromagnetic wave polarized parallel induces free movement of electrons along the length of the wire, generating a current on the metal surface and energy loss due to joule heating, whereas the remaining wave is reflected. In case of perpendicular polarization, the electron mobility is limited by the width of the wires. There is a negligible amount of the energy both lost and reflected. Thus most of the incident wave is transmitted through the grid. Therefore WGPs can be utilized as polarizers or polarizing beam splitters. The effectiveness of WGPs depends on the relationship between periodicity and wavelength, while the spacing between wires and their widths specify the application wavelength.

A schematic diagram of the WGP is shown in Fig. 2.2. Material properties are represented by their

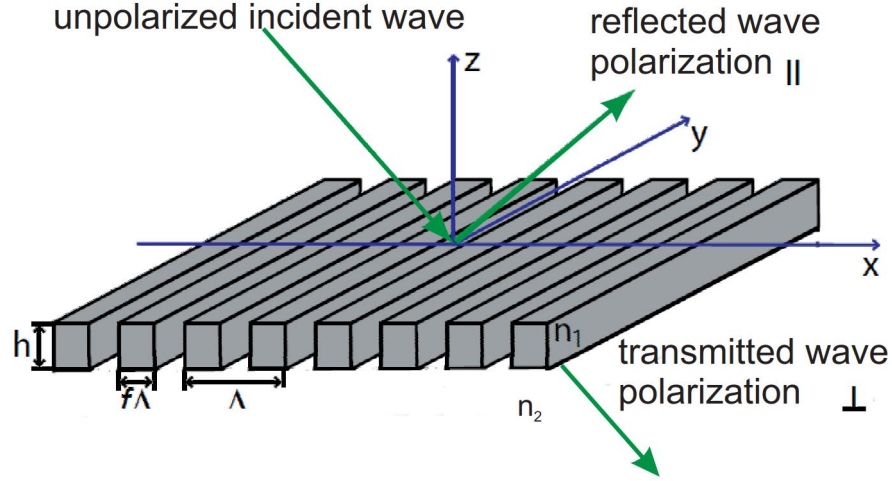


Figure 2.2.: Subwavelength wire grid polarizer: When an unpolarized wave is incident on the WGP, polarization parallel (\parallel) to the wires is reflected, while perpendicular polarization (\perp) is transmitted. The effectiveness of the WGP depends on dielectric contrast, which is described via the complex refractive index for the metallic wires and dielectric medium n_1 , n_2 , respectively, the metal fill factor f , grating period Λ and -height h .

refractive indices: n_1 is the complex refractive index for the metallic wires, n_2 is the refractive index of the dielectric medium; f stands for the metal fill factor, Λ is the grating period ($\Lambda \ll \lambda$, λ - wavelength of illumination wave) and h is the grating height. The first attempt to apply the effective medium theory to the analysis of WGP was reported by Yeh et al. [Poc77] and Yeh [Poc78, Poc81]. The authors proposed that a periodic layered medium consisting of layers of different homogeneous and isotropic materials following in sequence behaves as a uniaxial birefringent medium. The effective refractive indices of this composite structure are given by [Poc78]

$$n_{\text{TE}} = \sqrt{f n_1^2 + (1 - f) n_2^2} \quad (2.2)$$

$$n_{\text{TM}} = \sqrt{\frac{f}{n_1^2} + \frac{(1 - f)}{n_2^2}} \quad (2.3)$$

The lower indices TE and TM correspond to the polarization of the electromagnetic field with respect to the orientation of the metallic wires.

2.1.2. Complementary metamaterials and Babinet's principle

Babinet formulated a principle relating the diffraction from a perfectly conducting infinitely thin screen and its complement [Bab37]. The sum of the complex amplitude of the diffracted signal observed after a screen and its complement are the signals amplitude in presence of no screen. This is the scalar form of Babinet's principle, however an analogous theorem, extending its use to that

2. Theoretical background

of vectorial EM fields was derived by Booker in 1946 [Boo46].

The complementary field $\mathbf{E}_0^c, \mathbf{B}_0^c$ of an incident electric field \mathbf{E}_0 , \mathbf{B}_0 , is defined as

$$\mathbf{E}^c = -c\mathbf{B}_0 \quad \text{and} \quad \mathbf{B}_0^c = \mathbf{E}_0/c, \quad (2.4)$$

which corresponds to a 90° rotation $(\mathbf{E}_0^c, \mathbf{B}_0^c)$ around the propagation axis. The full vectorial formulation of Babinet's principle states that the field \mathbf{E}^c , \mathbf{B}^c behind a complementary screen illuminated by a complementary field $\mathbf{E}_0^c, \mathbf{B}_0^c$ is given by

$$\mathbf{E}^c = \mathbf{E}_0^c + c\mathbf{B} \quad (2.5)$$

$$\mathbf{B}^c = \mathbf{B}_0^c - \mathbf{E}/c, \quad (2.6)$$

where \mathbf{E} and \mathbf{B} are the scattered fields behind the positive structure. The total fields behind the structure are the superposition of the incident and the scattered fields. The total electric field behind the structure ($z > 0$) can be considered a duplicate of the total magnetic field behind the screen and vice versa

$$\mathbf{E}^c = c\mathbf{B} \quad \text{and} \quad \mathbf{B}^c = \mathbf{E}/c. \quad (2.7)$$

Note that on the left-hand side of the screen ($z < 0$) the scattered fields have opposite sign to ensure, that both the total magnetic polarization perpendicular to the screen and the total electric field polarization parallel to the screen vanish, as required for a perfectly conducting surface at ($z = 0$). From (2.6) it follows that the total electric field of a SRR, \mathbf{E} , and the total magnetic field of the CSRR, \mathbf{B}^c , in the region behind the structure ($z > 0$) are related by $\mathbf{E} + c\mathbf{B}^c = c\mathbf{B}_0^c$. Therefore, the transmission coefficient t^c for the CSRR illuminated by the complementary wave in (2.4) is related to the transmission coefficient t for the SRR by

$$t + t^c = 1. \quad (2.8)$$

Instead of utilizing the complementary, its possible to rotate the complementary structure by 90° , which in the experiment is realized through the SLM.

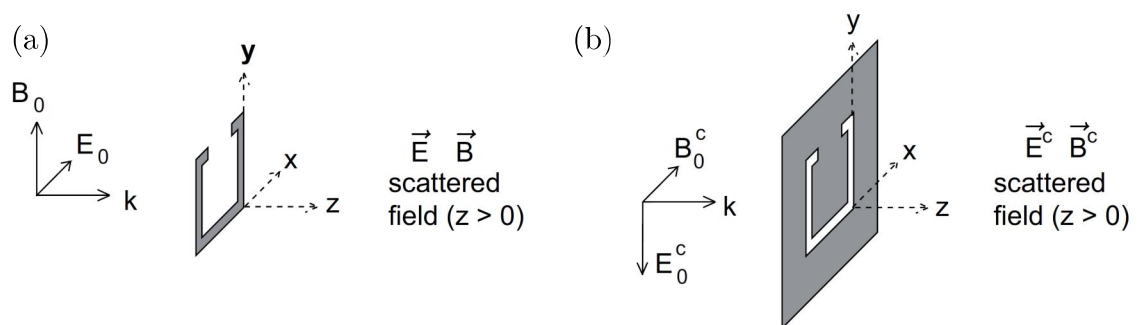


Figure 2.3.: Illustration of Babinet's principle which, relates the scattered fields \vec{E} , \vec{B} and \vec{E}^c , \vec{B}^c behind complementary perfect electrical conducting structures. Split-ring-resonator (a) and its complementary screen (b) illuminated by complementary incident fields.

2. Theoretical background

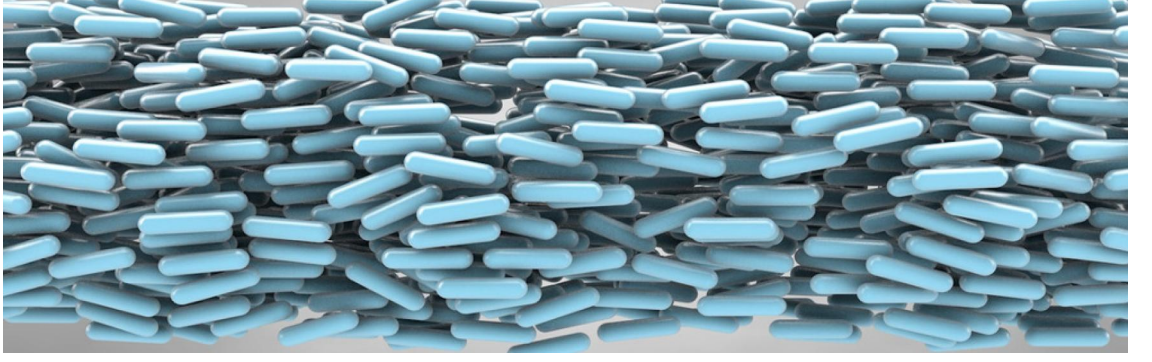


Figure 2.4.: Artificial illustration of nematic liquid crystals. These rod-shaped organic molecules have no positional order, but a self-aligned long-range directional order with their long axes roughly parallel. The majority of nematics are uniaxial i.e. one axis is longer and preferred, while the other two being equivalent, making the LC birefringent. Picture taken from [Lia15].

2.2. Patterned photo-excitation

2.2.1. Spatial light modulator

The creation of a dynamical controllable spatial confined illumination necessitates precise position dependent filtering capabilities. These will be realized through pixel-wise polarization modulation via a computer controlled spatial light modulator. The SLM consists of liquid crystal pixels. LCs are matter in a thermodynamic stable phase characterized by anisotropy of properties without the existence of a three-dimensional crystal lattice. Typical properties are cigar-like molecular structure, rigidity of the long axis, and strong dipole or easily polarizable substituents. The nematic phase is characterized by long-range orientational order, i.e. the long axes of the molecules tend to align along a preferred direction, but only short-range positional order, as shown in figure 2.4. The overall preferred orientational axis is defined by a vector $\mathbf{n}(r)$, which is called director, even though the locally preferred direction may vary throughout the medium.

Due to the uniaxial character of LCs, the dielectric susceptibility of a nematic is characterized by two components ε_{\parallel} and ε_{\perp} , which are the susceptibilities along and perpendicular to the long axis respectively. Correspondingly, we can introduce ordinary $n_o = \sqrt{\varepsilon_{\perp}}$ and extraordinary refractive index $n_e = \sqrt{\varepsilon_{\parallel}}$ as can be seen in figure 2.5(a). When light propagates through a birefringent medium with the polarization directions deviating from the birefringent axes, both field components respond to another susceptibilities. Therefore, the polarization state changes during propagation due to the change in relative phase of the two linearly polarized components. The modulation depends on sample length and strength of birefringence, which can be utilized for spatial light shaping. While the (ordinary) refractive index for an electric field along the short axis remains constant, the effective extraordinary refractive index

$$\varepsilon_{\text{eff}} = \frac{\varepsilon_{\perp} \varepsilon_{\parallel}}{\varepsilon_{\perp} \cos^2 \theta + \varepsilon_{\parallel} \sin^2 \theta}. \quad (2.9)$$

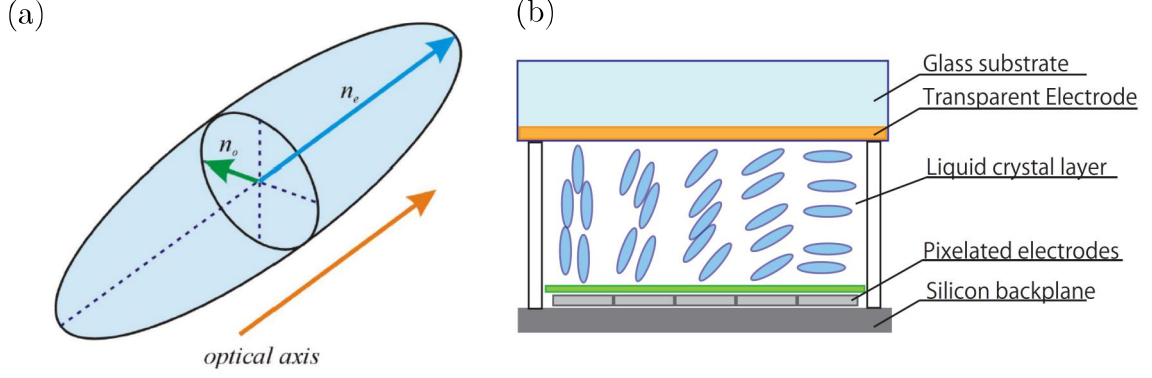


Figure 2.5.: (a) The uniaxial character of LC induces a birefringence, modulating a propagating electromagnetic wave depending on its polarization direction in either phase or polarization. (b) Cross-section of SLM device with multi-layer structure. This device is equipped with an active-matrix silicon circuit on the backplane, allowing electrical control over orientation order of the parallel-aligned nematic LC layer. Additionally, the backplane serves as a reflective plane by depositing a dielectric mirror layer on the surface. Pixelated metal electrodes were fabricated on the active-matrix circuit with HD resolution (1920×1080 square pixels) and high fill factor (91%). The LC layer is sandwiched in between alignment layers attached to a glass substrate via transparent electrodes. Picture (a)/(b) taken from [Bur16, Tak14].

for an electromagnetic wave depends on the angle θ between electric field and long axis of the crystal. The polarization modulation is therefore determined via the angle between incident electric field and director. While a linear polarized field parallel/perpendicular to the director only experiences a phase shift, any angle in between leads to a polarization modulation.

By applying an electric field, the director changes its orientation and aligns along the electric field, giving direct control over the angle between field and director. Consequently, the effective refractive index and therefore the strength of birefringence change. This phenomenon is utilized in a spatial light modulator (SLM) for beam shaping. As shown in figure 2.5(b), this device consists of 1920×1080 pixels, which contain parallel aligned nematic liquid crystals. A voltage can be applied to each pixel separately, whereby the effective refractive index of the display can be varied pixel-wise. An incoming beam, that propagates through the translucent pixels, experiences a voltage dependent spatial polarization modulation and will be reflected by the dielectric mirror beneath. By passing through a filter, the polarization modulation can be translated into an amplitude profile.

2. Theoretical background

2.2.2. Properties of photo-excited semiconductors

In an unoccupied semiconductor all electrons are bound in the valence band, prohibiting all flow of charge, making the semiconductor insulating [Ash76]. On the contrary, free charge carriers in the conduction band allow the semiconductor to conduct electrical charge. The ability to control the electron conductivity is one of the key properties of semiconductors. This control can be achieved by exciting carriers from the valence band to the conduction band through thermal- [Yac03], photo-excitation [Kam14, Oka10], chemical doping [Sch15] or electrical injection of charge carriers [Che08a]. In this thesis, the accessible electron conductivity via photo-excitation is used to generate a charge carrier distribution, allowing control of transmitted THz radiation.

To estimate the spatial conductivity and tailor it accordingly, we apply the Drude model. In this model conduction electrons are assumed to behave as a gas of freely moving charges. This movement is constantly randomized by collisions with imperfections and defects in the lattice, leading to velocity relaxation. The material permittivity as a function of the conductivity induced by free charge carriers can be derived from the Maxwell's equations. The relative complex permittivity ε depends on frequency and carrier density as per

$$\varepsilon(x, y, \omega) = n^2(x, y, \omega) = \left(1 - \frac{\omega_p^2}{\omega^2 + \frac{i\omega}{\tau}}\right) n_\infty^2 \quad (2.10)$$

where τ is the mean collision time of the charge carriers.

Since free electrons are charged and delocalized, they can be described from an electromagnetic point of view as a plasma. A plasma can be driven into a coherent oscillation, where the natural resonance occurs at the plasma frequency

$$\omega_p = \sqrt{\frac{Ne^2cZ_0}{m^*n_\infty^2}} \quad (2.11)$$

The screened plasma frequency is determined by carrier density N in the conduction band, elementary charge e , light velocity c , free-space impedance $Z_0 = 377\Omega$, unexcited refraction index n_∞ (e.g. Si: $n_\infty = 3.42$) and the effective mass m^* of the conduction electrons, which depends on the band-structure of the conductors (e.g. for SI approximately 0.26 times the free-electron mass). By sufficiently strong photo-excitation of a semiconductor, the plasma frequency ω_p becomes larger than the probe frequency ω , therefore n assumes a large imaginary part, implying strong attenuation and metallic behavior. Combined with the spatial light control mechanism introduced in the previous section, a tailored refraction index landscape can be produced.

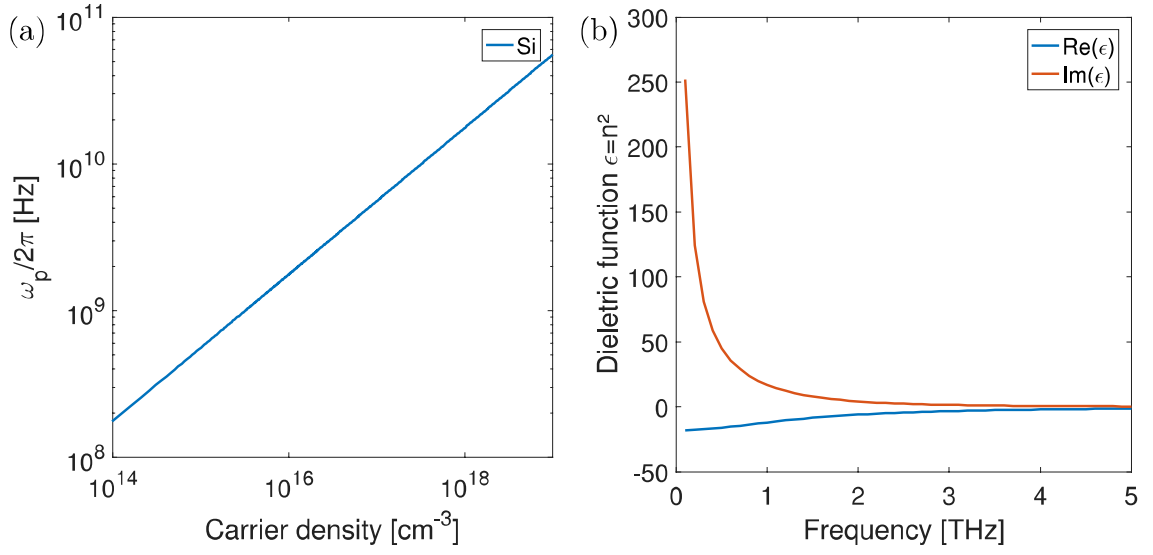


Figure 2.6.: (a) Plasma frequency ω_p of Si for different carrier concentrations. (b) Relative complex permittivity ϵ for Si as a function of frequency. All Curves are calculated with the Drude model using parameters as mentioned in the text.

3. Experimental details

In the second part of this thesis, the experimental prerequisites for a transient THz modulation are introduced and explained. As described in chapter 2.2.2, illuminating a semiconductor with photons of energies exceeding the bandgap, induces electron-hole pairs that contribute to the conductivity. The pump pulses, containing these photons, are generated by a Ti:Sapphire oscillator and two stage amplifier system. When projecting an image on the semiconductor, this image will be converted into a spatial profile in the local concentration of charge carriers. Within short timescales, induced charge carriers are confined to these illuminated areas, leading to a local permittivity contrast. The photo-generation of THz wire grid polarizers on Si was recently demonstrated by Kamaraju and coworkers by illumination through an optical mask [Kam14]. In the following the laser system, optical imaging, THz generation and detection will be explained in detail.

3.1. Laser system

A laser oscillator is based on an optical cavity/resonator and an active medium, which coherently amplifies light by stimulated emission. For amplification, the active medium must exhibit population inversion, which can only be achieved through an external energy supply. In this work, a titanium-doped sapphire crystal (Ti:sapphire) is optically pumped by a pulsed frequency-doubled Nd:YAG (neodymiumdoped yttrium aluminum garnet; $\text{Nd:Y}_3\text{Al}_5\text{O}_{12}$) laser at 532nm. The ultra-short pulses of the Ti:sapphire laser (approx. 8 fs) with pulse energies of 6.5 nJ at a repetition rate of 80 MHz are generated through mode locking. The resonance frequencies (modes) of the resonator within the gain spectrum of the Ti:sapphire crystal (roughly 670 to 1100 nm [Spe91]) are interconnected through a fixed phase relation. In Ti:sapphire, passive mode locking occurs via Kerr lensing, which is a third order non-linear optical effect, causing stronger amplification for intensive parts of the pulse. The output is then in a 3:1 ratio. The stronger part is used as the seed for further amplification, while the weaker part is required for the electro-optic sampling within the THz detection, which will be explained in an adjacent chapter.

A two stage amplifier system is used to enhance the stronger part of the oscillator pulse from nJ to mJ energies. First, the 8 fs seed pulses are stretched to a pulse length of picoseconds to minimize the influence of higher order non-linear effects due to too high peak intensities in the amplification process. Otherwise, these effects would distort the pulses or even lead to damaging optical elements. The first amplification stage consists of two Ti:sapphire crystals. By reducing the repetition rate to 1 kHz, the limited output power of the crystal (1-10 W) is bypassed. One crystal is operated in a regenerative mode, in which the laser pulse passes several times through

3. Experimental details

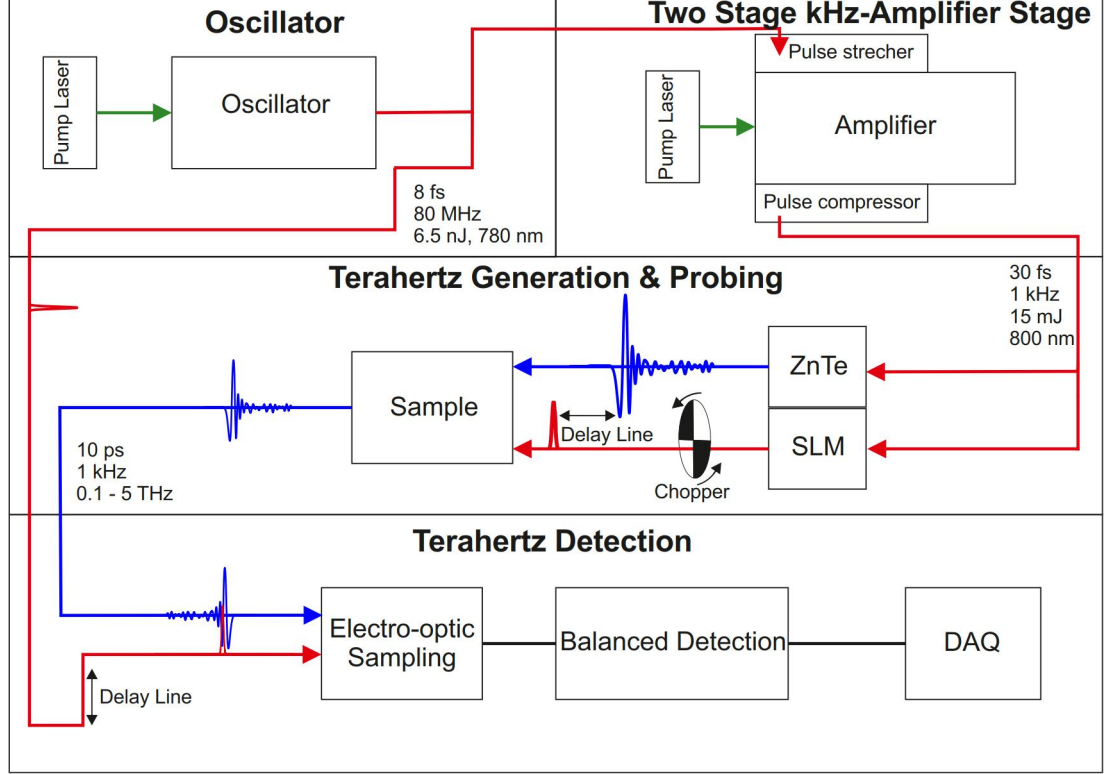


Figure 3.1.: An oscillator generates femtosecond pulses with a central wavelength of 780nm (red lines) at a repetition rate of 80 MHz. These pulses are sent to a pulse stretcher before they enter two amplification stages, after which they traverse a pulse compressor. Only a part of the 80MHz pulse train is amplified, which results in a reduction of the repetition rate to 1 kHz. Part of these NIR pulses with a wavelength offset are mixed in a non-linear crystal, such as ZnTe, leading to an optical rectification process, while the other part is used for photo-exciting the semiconductor. The generated picosecond THz pulses (blue lines) and a part of the oscillator pulse co-propagate through the studied sample to a detection crystal to record the THz time trace via electro-optic sampling. The THz pulse induces a birefringence that changes the polarization of the co-propagating 780nm gate pulse. In the balanced detection stage, two photo diodes record the change of the state of polarization of the gate pulse. Subtraction of two subsequent photo diode differences, and an additional amplification of the signal with a boxcar unit and a computer (PC), yields the electric field of the THz transient as a function of time.

the Ti:sapphire crystal, where at each subsequent trip the pulse energy increases. The other crystal works in a single pass mode. After this first amplification stage, the stretched pulses hold a pulse energy of 10 mJ at a repetition rate of 1 kHz. In the second amplification stage, a Nd:YAG laser pumped Ti:sapphire crystals is used in single pass mode. To avoid thermal lensing, the crystal is cooled with liquid helium to roughly 60-70 K. After splitting the output in two equal parts, the process is concluded as each part is sent into their own compressor, reducing the pulse duration to 40 fs. The overall output is two 800 nm beams with a combined pulse energy of 15 mJ at a repetition rate of 1 kHz.

3.2. Imaging setup

Photo-excitation of semiconductors allows direct control over the complex refractive index. However, metamaterials utilize their small size and periodicity to form an effective homogeneously modulation. To exhibit the aspired modulation, the single unit cell has to be tailored precisely, requiring a high quality projection setup.

A polarized pump beam is sent in reflection through a polarizing beam splitter (PBS), after which the beam impinges at normal incidence on a spatial light modulator. On the return pass through the PBS, only pixels, which have rotated the polarization of the pump, will be transmitted by the PBS, directing this light onto the sample.

The resolution of the projected image is limited by the pixel size of the SLM, which is $8 \times 8 \mu\text{m}^2$. This is highly sub-wavelength at THz frequencies and can be further improved through demagnifying optics. The modulation of terahertz radiation via photo-generated metamaterials requires high imaging resolutions, therefore one of the goals to get diffraction-limited performance. Perturbations such as optical aberrations, electric cross-talk of pixel and display curvature of the SLM have to be well known and minimized. In the following, possible problems are discussed and the quality of the spatial confinement is characterized and optimized.

Optical aberrations and local image quality

A useful technique to determine the response of a system is the transfer function. To measure the imaging quality of a system, the point spread function (PSF) is utilized. The PSF or impulse response describes how a point source is imaged by the projection system. The degree of spreading (blurring) of the point object is a measure for the quality of an imaging system. In practice the shape of the PSF is often a combination of multiple optical effects, including diffraction, aberration, defocus, and etc. Figure 3.2 illustrates six of the most typical optical effects and their corresponding PSFs. The five basic types of aberration due to geometry of lenses, mirrors, which are applicable in a monochromatic system are known as Seidel aberrations. Furthermore, aberrations due to dispersion ($\partial n / \partial \omega \neq 0$) have to be considered.

Astigmatism is an anisotropic effect that gives rays in two perpendicular planes different foci. Vertical and horizontal elements are in sharp focus in two different planes. Astigmatism errors are corrected by designing the system to provide precise spacing, shapes and indices of refraction for individual lenses.

Comatic aberrations describe a variation in magnification over the entrance pupil, so that it affects off-axis points on the object. It leads to a comet-like tail. The comatic aberration of lens or a system can be minimized by matching the curvature of the lens surfaces to the application.

The focal length is dependent on the refractive index, resulting in a failure to focus all wavelengths to the same convergence point. These chromatic aberrations manifest themselves as fringes of color along boundaries of dark and bright areas of the image. While monochromatic light is not affected, the spectral broadband nature of femtosecond pulses, demands correction of chromatic aberrations. Otherwise no precise photo-excitation can be warranted. An achromatic lens, which

3. Experimental details

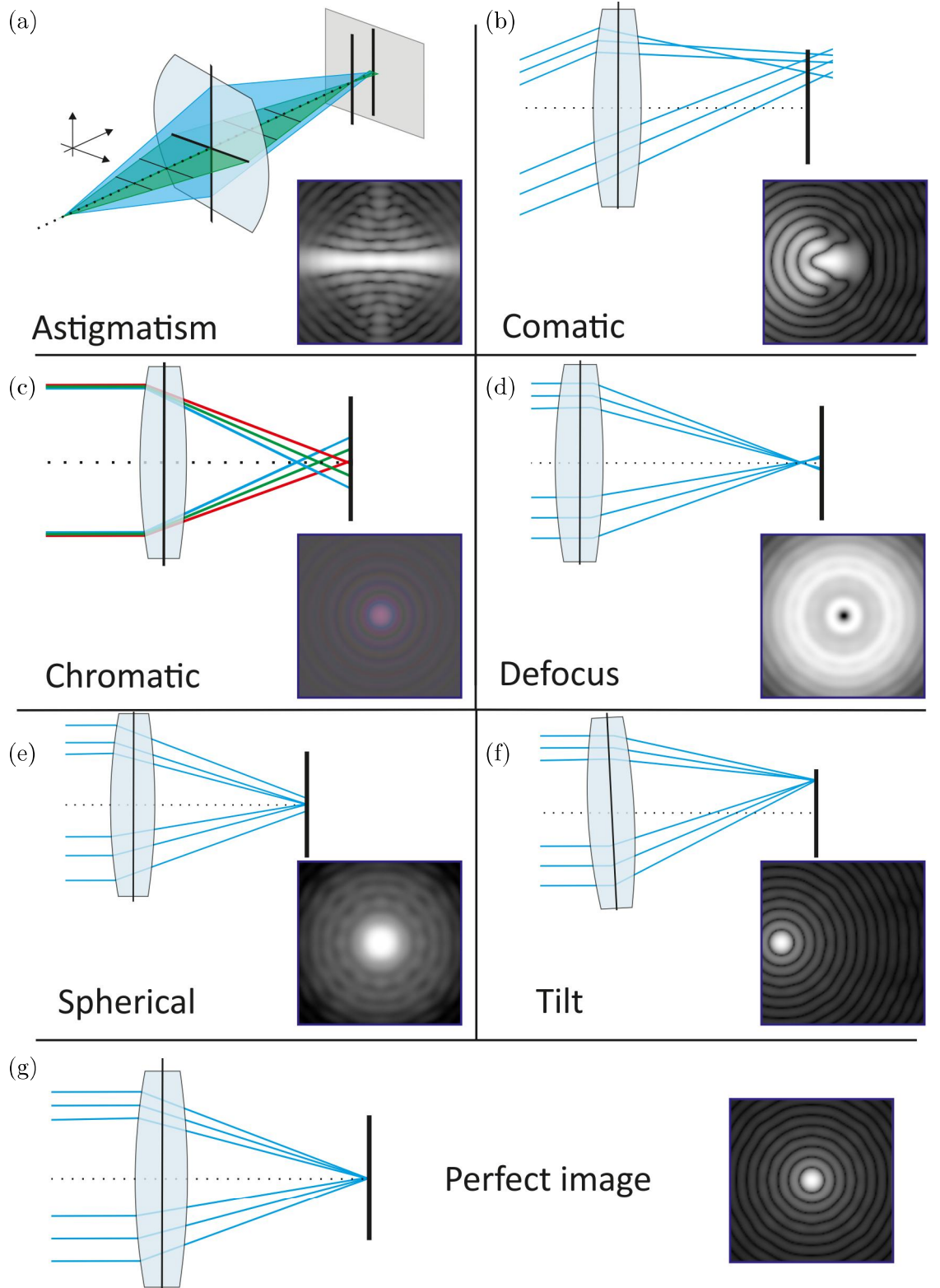


Figure 3.2.: Illustrate of six of the typical optical aberrations, which are corrected in the used projection setup, and their resulting PSFs (simulated). (a) Astigmatism leads to two different focus planes for perpendicular rays. (b) Comatic aberrations result from a variation in magnification and manifested in comet-like tail. (c) Chromatic fringes are created due to dispersion. (d) Defocus describes a displacement of the focus plane. (e) Spherical surfaces cannot create a perfect spherical phase profile, resulting in different focus planes. (e) Tilt leads to a displacement of the focus position, not the plane. (f) shows diffraction limited optimal imaging.

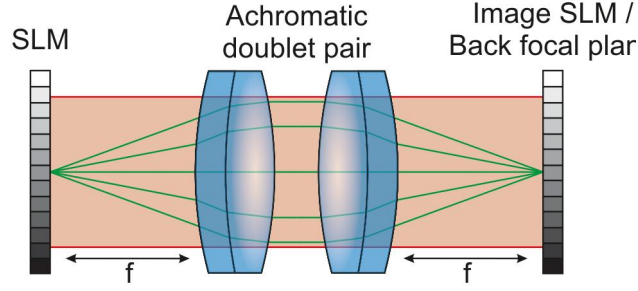


Figure 3.3.: Utilized 2f imaging system for projection of the SLM onto the semiconductor sample. An achromatic matched lens pair avoids the image distortion due to plasma fluctuations, while minimizing chromatic aberrations. Furthermore the lenses are matched for demagnification, increasing the possible pump intensity and enabling smaller metamaterial structures.

consists of multiple cemented lenses with different amount of dispersion, allows counterbalancing of the chromatic aberration.

A more obvious kind of aberration is defocus. Defocus means that wave fronts are converging properly, but not to a point in the desired plane. The concept of defocus can be extended to a displacement in the transverse direction. This can be fixed by adjusting the focus length of the lens system, or re-positioning the setup.

In contrast to 1st order geometrical optics, spherical surfaces do not create a perfect spherical phase profile. The result is, that rays parallel to the optical axis at different radii will have different focal planes. These aberrations are called spherical. Like chromatic aberrations the shape and composition of achromatic lenses can be used to limit the effects of spherical aberration.

Since the direction of propagation is defined by the normal vector to the phase front, tilting the phase front will change the location of the focal point. A tilt corresponds to a linear slope. It is not considered a real aberration, since it does not bend the wave fronts. Tilt aberrations can be fixed by realigning the wave front, this can be done by adjusting in-coupling mirrors.

To compensate for most aberrations, modern lens design applies lenses of different shapes and materials [RA15,Kem92,Kem93]. to get diffraction-limited performance. Diffraction occurs because light as a wave will bend around obstacles and spread past them. The shape of diffraction PSF of a circular aperture is referred to as airy disk, as shown on the bottom in figure 3.2. As shown in figure 3.3, a matched achromatic doublet pair is utilized in this experiment to reduce optical aberrations and map the SLM in a 2:1 ratio onto the sample for improved sub-wavelength studies. A single SLM pixel ($8\ \mu\text{m}$ pitch) gets demagnified in a 2:1 ratio illuminating roughly $4\ \mu\text{m}$ area. A conventional telescope of two lenses would allow demagnification, but the intensity of the pump pulse are sufficient high to generate a plasma in each focus spot, that would significantly change the projected image due to plasma fluctuations. While a single biconvex lens would avoid this, the achromatic doublet pair offers the advantages of achromatic lenses, while preventing a focus spot between both lenses.

Alongside the imaging conditions, the focus size of the incident THz radiation on the sample has to be considered, whose FWHM has been measured as 1.3 mm. The incoming optical beam has a beam

3. Experimental details

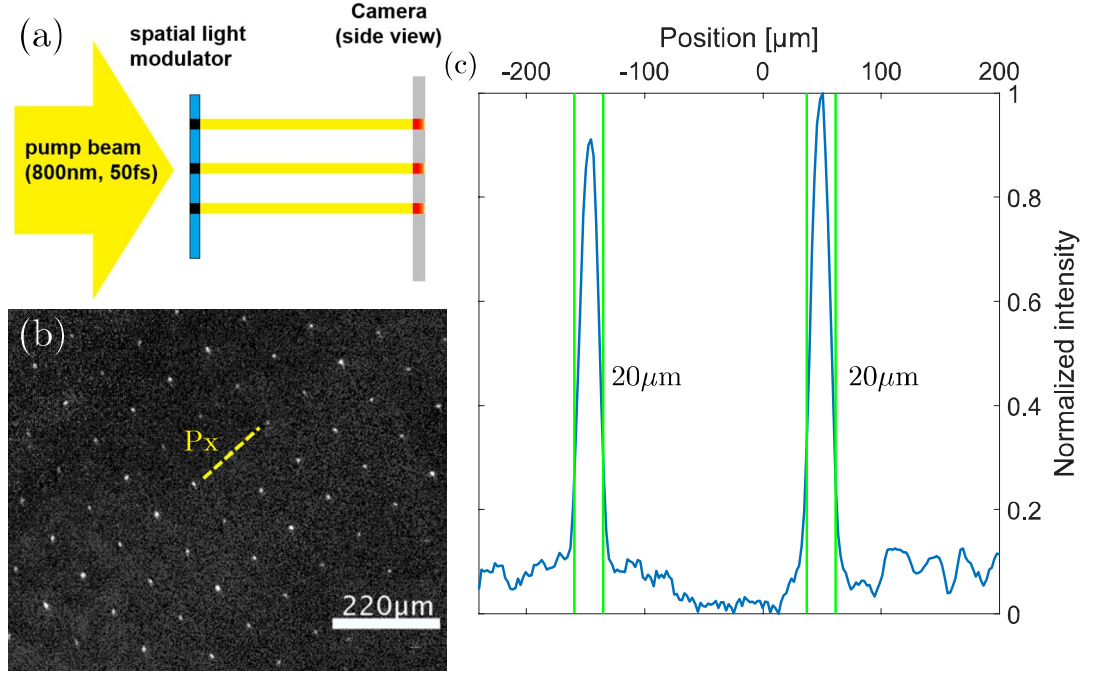


Figure 3.4.: Figure (a) shows how the SLM projects a generated $16 \times 16 \mu\text{m}$ area onto the camera. (b) shows the recorded intensity image of the camera, while also showing the line profile along which the intensity profile in (c) is taken. The FWHM of this profile is $20 \mu\text{m}$.

waist of 10 mm before demagnification, resulting in 5 mm on the sample. Further demagnification would increase the modulation capabilities through smaller more intense structures, but would risk the overlap with the THz spot, while this setup guarantees homogenous illumination of the THz focus.

By placing a CCD camera in the position of the sample and generating a $16 \times 16 \mu\text{m}$ area on the SLM (cf 3.4(a)), the point spread function of the system can be estimated. Therefore, the recorded intensity image is evaluated along a line profile as shown 3.4(b). The result is depicted in figure 3.4(c). The FWHM of the bright pixel areas is underlined by green lines and is $20 \mu\text{m}$. The increased size shows the finite quality of the SLM pixel technique. While the phase shift of distant pixels can be different, neighboring cannot have a drastically different phase shifts due to voltage crosstalk between the pixels. Furthermore, dirt, dust and other particles on the neutral density filter, which is placed in front of the camera to hinder saturation/damage due to high intensities, degrade the image quality through diffraction. For more detailed evaluation of the image quality also see A.5.

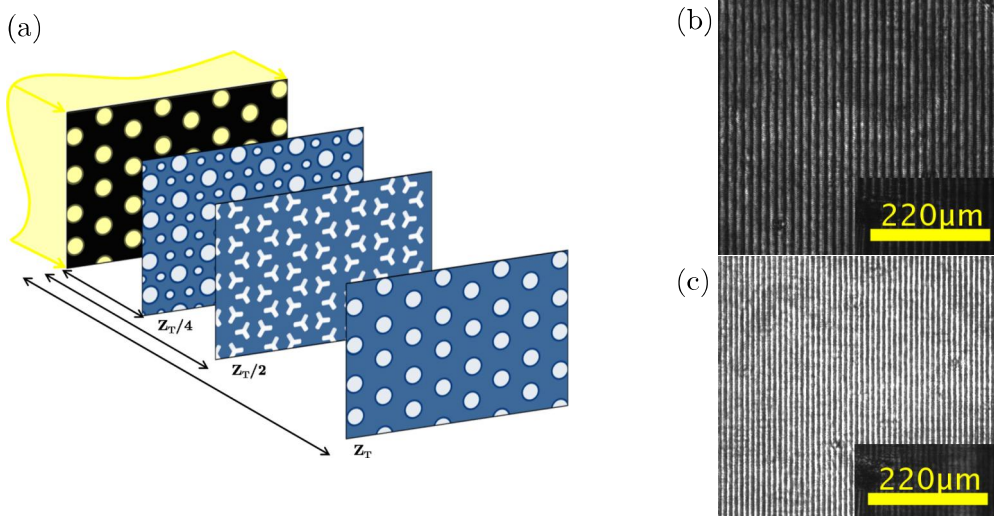


Figure 3.5.: (a) Schematic representation of the Talbot effect, which leads to periodic sub-image decreased in size at fractions of the Talbotlength. (b) Utilized wire-grid pattern for THz modulation. (c) Talbot sub-image for a wrongly positioned lens/sample.

Talbot effect

The Talbot effect is a diffraction effect first observed in 1836 by Henry Fox Talbot. When a plane wave is incident upon a periodic diffraction grating, the image of the grating is repeated at regular distances away from the grating plane. This distance is called the Talbot length, and the repeated images are called Talbot images. Furthermore, at half the Talbot length, a self-image also occurs, but phase-shifted by half a period. At smaller regular fractions of the Talbot length, sub-images can also be observed creating a fractal pattern of sub-images with ever decreasing size, often referred to as a Talbot carpet (cf 3.5(a)). The Talbot effect is a natural consequence of Fresnel diffraction and the Talbotlength can be found by the following formula

$$z_T = \frac{2a^2}{\lambda}, \quad (3.1)$$

where a is the period of the diffraction grating and λ is the wavelength of the light incident on the grating. However, this formula is only valid for the sub-wavelength gratings.

The original wire grid polarizer in figure 3.5(b) has a period of $32 \mu\text{m}$. At an incident plane wave of 1 THz, this leads to a Talbot length of roughly $9 \mu\text{m}$. This rather short length seems negligible compared to typical positional displacement ($\approx \text{mm}$), but especially because of the finite imaging quality of the SLM the effect was initially not distinguishable from the real image. While maintaining the overall shape, the Talbot WGP appeared with a $2/3$ decreased unit cell size, as can be seen in fig. 3.5(c). While the increased intensity looks beneficial at first, the Talbot length differs for variations in periodicity and unit cell size, limiting the applicable patterns. Therefore, precise alignment of the sample position via μm -translation stage is used to compensate the Talbot effect.

3. Experimental details

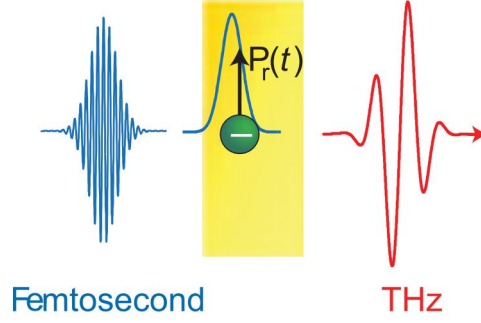


Figure 3.6.: Optical generation of THz transients. Optical rectification. An intense femtosecond pump pulse inside a non-inversion-symmetric transparent crystal induces a charge displacement with a rectified component $\mathbf{P}_r(t)$ that roughly follows the intensity envelope of the pulse (blue curve in yellow crystal). $\mathbf{P}_r(t)$ acts as a source of a THz electromagnetic transient. This figure is taken from [Kam13].

3.3. Terahertz generation and detection

Terahertz generation

The first experimental demonstration of THz optical rectification by Zernike and Berman in 1965 [Zer65] utilized difference frequency mixing in the near-infrared in quartz and achieved THz-radiation generation at 3 THz. Since almost four decades optical rectification (OR) has been a basis for especially broadband single-cycle THz pulses. In general, optical rectification refers to the rise of a DC or low-frequency polarization when intense laser beams propagate through a crystal. OR is a second order non-linear optical process. The electric polarization P of a material is proportional to an applied electric field E and its electric susceptibility χ . Expanding the susceptibility in powers of the electric field E describes the non-linear optical response.

$$P = (\chi_1 + \chi_2 E + \chi_3 E^2 + \chi_4 E^3 + \dots)E \quad (3.2)$$

Second order non-linear optical effects like optical rectification and the linear electrooptic effect, which will be used for the detection setup, occur only in non-centrosymmetric crystals. Furthermore generation and detection crystal require sufficient transparency at THz and optical frequencies. Considering an oscillating electric field $E = E_0 \cos(\omega t)$ the second-order non-linear polarization

$$P_2^{\text{NL}} = \chi_2 E^2 = \chi_2 \frac{E_0^2}{2} (1 + \cos(2\omega t)) \quad (3.3)$$

consists of a rectified polarization $\chi_2 E_0^2/2$ and a polarization with a $\cos(2\omega t)$ dependence, which describes the second harmonic generation. The induced OR polarization will act as a source, radiating off a single cycle pulse as shown in figure 3.6. Using short pulses and therefore spectral broad light instead of spectral narrow continuous waves, the EOR component is broadened in frequency space around $\omega = 0$. Sufficient short pulses expand the broadening into the THz regime.

EOR can be viewed as a degenerate case of difference-frequency generation for identical frequencies. Ideally, the generated THz radiation and the NIR pulse are phase matched viz they propagate at the same speed through the crystal. In this vein, the emitted THz waves add up coherently throughout the whole crystal leading to highest conversion efficiency. Furthermore, the strength of the radiation for all frequencies within the bandwidth increases with crystal thickness. Phase matching requires a non-linear crystal, whose group velocity for the femtosecond laser pulse is identical to the phase velocity of the THz radiation. However, NIR group velocity and THz phase velocity are generally not identical. Consequently, the efficiency of OR decreases if the mismatch caused by long propagation within the crystal becomes too large. In principle emission strength and bandwidth have a reciprocal relationship regarding crystal thickness. Emission strength increases with thickness, while bandwidth decreases and vice versa.

Terahertz detection

A useful technique for detecting THz radiation is electro-optic sampling (EOS), which allows direct detection of the electric field in the time domain. The THz transient (duration > 100 fs) is overlapped with a 8 fs oscillator gate pulse (cf. 3.7(b)). Using a silicon wafer, which is nearly transparent for THz radiation and reflective for NIR, both pulses copropagate through a non-linear optical crystal, such as ZnTe. In the crystal, the THz pulse induces a birefringence via the Pockels effect, which is also called linear electro-optic effect and proportional to the THz electric field amplitude. The induced birefringence retards the phase of the NIR gate beam and alters its polarization of initially linear to elliptic. The phase retardation

$$\Gamma \propto \frac{1}{\lambda_{\text{Gate}}} l n^3 r_{41} E_{\text{THz}} \quad (3.4)$$

is proportional to the amplitude and phase of the terahertz electric field E_{THz} , the crystal thickness l , the linear electro-optic coefficient r_{41} , the refractive index of the crystal at the wavelength of the gate beam n and the wavelength of the gate beam λ_{Gate} . The phase shift can be measured via a balanced detection setup, which consists of a quarter-wave plate, a Wollaston prism (WLP), and two balanced photodiodes as shown in figure 3.7(a). The Wollaston prism separates the gate pulse into two mutually orthogonal polarization components, which are detected by the balanced photodiodes. Without THz signal, the balanced diodes measure exactly the same intensity, which can be aligned through the quarter-wave plate. Before the signal is sent to the processing system, it gets amplified by an electrical amplifier.

The signals of both balanced photodiodes are subtracted from another, canceling any intensity fluctuation of the probe beam. By delaying the ultrashort fs NIR pulse with respect to the THz radiation, the temporal profile of the THz radiation is mapped out via measurement of phase retardation Γ as function of the delay (c.f. 3.7(b)). A motorized delay stage allows scanning of the delay time τ .

3. Experimental details

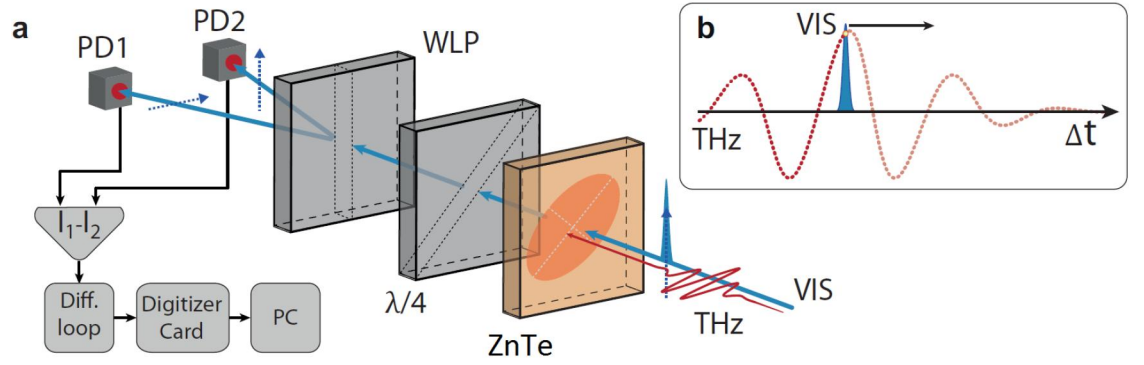


Figure 3.7.: (a) In electro-optic sampling, an intense THz pump pulse induces a birefringence in a non-linear crystal (ZnTe) via the Pockels effect. A co-propagating less intense gate pulse, whose delay can be varied, experiences a change in its state of polarization. This change in polarization carries the information of the electric field amplitude and phase of the THz transient. Using a balanced detection scheme, this change in polarization of the NIR pulse is detected using a wave plate, a Wollaston prism (WP) and two balanced photo diodes (PD1; 2). Subsequently, the signals from the two photo diodes are subtracted from each other and amplified with the help of a computer (PC). (b) With the help of a motorized delay stage, the delay time between THz and gate pulse can be varied to scan through the whole THz wave form. Picture taken from [Mä16].

4. Results and discussion

Terahertz (THz) time-domain spectroscopy is a powerful method for studying photo-excited meta-materials. In this chapter, the experiments and measured data are presented and discussed. The directly accessible electric field in the time-domain is used to characterize the response of the semiconductors following optical excitation. For the evaluation of the excited case, first the response of the material in the unexcited/unpumped state has to be known. Afterward, the time-domain spectrometer is combined with an optical pump pulse to homogeneously induce free charge carriers in the samples, which change their optical properties according to the Drude model. For this purpose, Silicon and Gallium arsenide are the materials of choice. The bandgap of Silicon ($375/5\ \mu\text{m}$) and GaAs ($500\ \mu\text{m}$) are 1.12 eV (1107 nm) and 1.42 eV (873 nm), respectively and are sufficiently large to prevent thermal excitation at room temperature, while allowing non-linear excitation of charge carriers through amplified 800 nm pulses. The Drude model and a simplified transfer matrix method are then utilized to characterize the free charge carrier generation. Furthermore the dynamics of these processes are studied via pump-probe measurements.

After this substrate characterization, periodic subwavelength structures, e.g. wire grid polarizers and rod antennas, are imprinted by pump pulse, thereby creating transient metamaterials in the semiconductor. To extract the optical properties of these induced structures, their TDS signal is compared to the unexcited sample. Via Fourier transformation, the optical properties such as transmission ratio and relative phase delay get accessible and provide frequency-resolved information. The transmitted THz transients are measured for various structures, structures sizes, periodicities, pump fluences, samples and THz polarizations.

4. Results and discussion

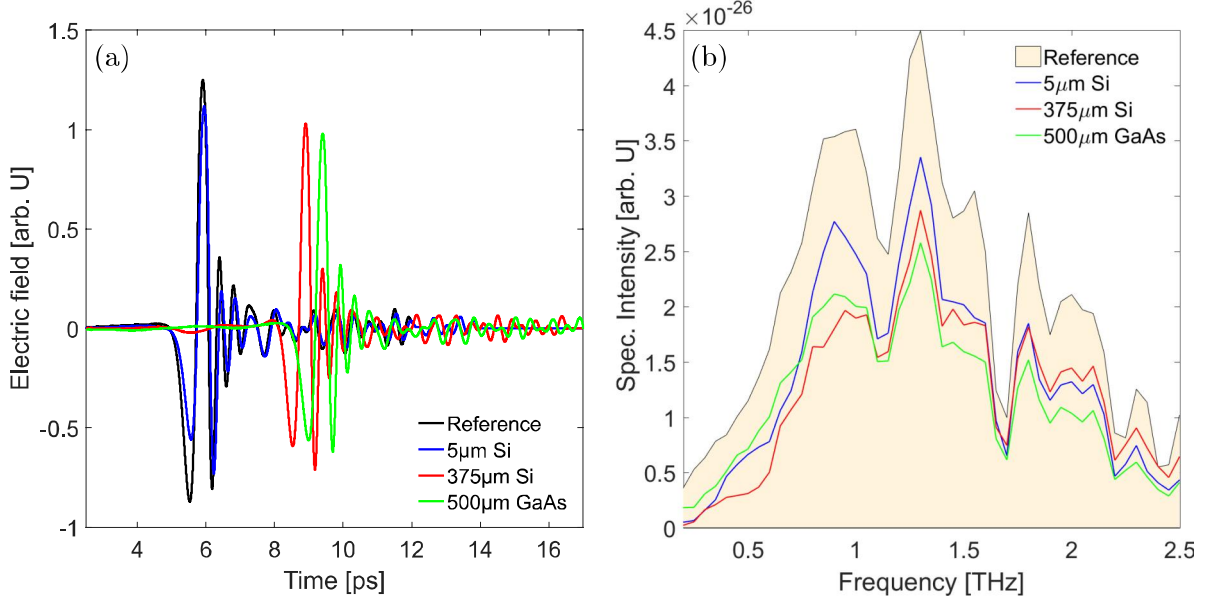


Figure 4.1.: Typical raw data: (a) Time-domain transients of THz pulses after transmission through a 5 μm Silicon sample (blue curve), a 375 μm silicon sample (red curve), a 500 μm GaAs sample (green curve). The reference signal without a sample is also shown (black). The corresponding intensity spectra are obtained via Fourier transformation and are shown in (b). The spectral response of the experimental setup without sample is represented by the fawn colored area.

4.1. Unexcited sample optical constants

Time-domain data

The THz-TDS setup described in the preceding section (see figure 3.1), permits the determination of the complex spatial modulation of a sample. To access these information, the setup has to be characterized. Therefore, the THz transmission through air is recorded. First this signal serves as a reference for the unaltered transmission properties of the time-domain spectrometer.

Once the reference response is known, the THz transients after transmission through the 5 μm and 375 μm silicon sample and 500 μm GaAs sample are recorded. Figure 4.1(a) shows the time-domain response of the THz-TDS spectrometer with the black curve, and the transmission through a 5 μm Silicon sample (blue curve), a 375 μm silicon sample (red curve) and a 500 μm GaAs sample (green curve). The amplitude is reduced by reflection and absorption-losses, while the delay in time is due to the reduced group velocity as a result of the refractive index of the semiconductors being larger than in air.

Fourier domain/spectral transmission

The spectral intensity of the electric fields is accessed via Fourier transformation, whereupon the time frame of the electric field has to be selected properly beforehand to avoid loss of information. This windowing is thoroughly discussed in appendix A.4. The Fourier amplitude is in general

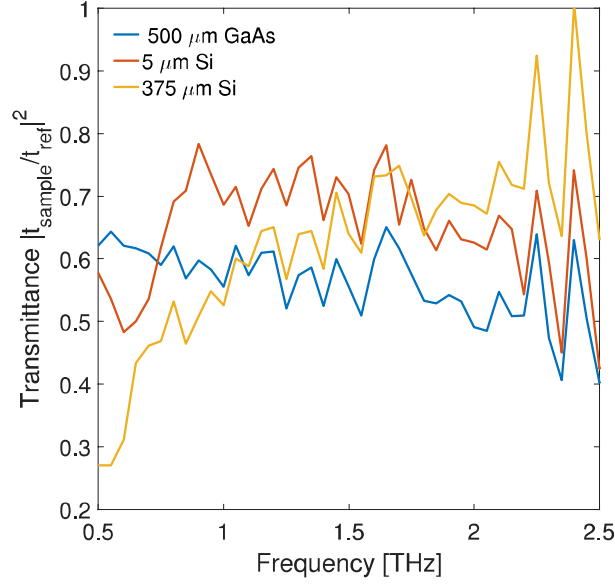


Figure 4.2.: Transmittance of unexcited samples: Transmittance spectra for 5 μm Silicon sample (red), 375 μm silicon sample (yellow) and 500 μm GaAs sample (blue). The curves represent the squared absolute of normalized Fourier transforms of the electric fields shown in figure 4.1.

complex, and its absolute square represents the intensity spectrum of the THz transient. For the semiconductors and reference, the intensity spectra are shown in figure 4.1(b). The intensity spectra are the result of both the characteristic response of the experimental setup and the sample transmission. For this reason the reference electric field was measured by normalization of the samples electric field to the reference signal, the characteristic response of the setup vanishes. The complex transmission of the sample is defined as

$$\tilde{t} = \frac{\tilde{E}_{\text{Sample}}}{\tilde{E}_{\text{Reference}}} = |\tilde{t}|e^{i\theta(\nu)}. \quad (4.1)$$

The two relevant properties of this response are the phase shift $\theta(\nu) = \arg\tilde{t}(\nu)$ and the transmittance $T = |\tilde{t}|^2$. The transmittance, depicted in figure 4.2, is expected to be constant, because of the negligibly varying refractive index in the THz regime. Only considering frequencies with amplitude $> 20\%$ of the maximum (0.7 to 2 THz), the transmittance can be considered as roughly constant.

4.2. Photo-excitation

Time domain

After characterizing the bare/unexcited samples, the semiconductors are illuminated homogeneously with the pump projection setup described in section 3.2 and then characterized with the THz-TDS. Analogous to the preceding experiment, the optical properties of the samples compared to a reference shall be measured. Here, we are interested in the change of transmission when the samples are photo-excited. Therefore the photo-excited transmitted fields are referenced to those of the unaltered samples.

As before the transmitted electric fields are measured with the EOS-setup. For direct comparability the pumped and unexcited semiconductor are measured simultaneously via a chopper. The pump-probe delay is set to 10 ps. All semiconductors are measured for the fluences 0.12, 0.25, 0.38, 0.5, 0.7 mJ/cm², respectively. The recorded electric fields for 5 μm Si, 375 μm Si and 500 μm GaAs are depicted in Fig. 4.3(a),(d) and (g). When photo-excited, the transmitted electric field decreases in amplitude. This trend is expected because a larger fluence excites more electron-hole pairs, which increases the metal-like behavior, resulting in reduced THz transmission.

Fourier domain

The Fourier transformation of the measured electric fields and the normalization to the unexcited samples gives access to the phase shift for 5 μm Si, 375 μm Si and 500 μm GaAs, which are plotted in figure 4.3(b),(e) and (h). An increase in pump fluence decreases the refractive index, shortening the optical path length. Therefore a stronger negative phase shift confirms the more metallic behavior. While the phase shift for the thin silicon sample is comparably flat, the other spectra show more pronounced features, especially for frequencies lower 0.7 THz.

The thick Si sample has a stronger decrease in transmission per fluence than the thinner Si sample. In appendix A.3, the power absorption of both silicon samples was calculated. While thick sample absorbs all of the entering pump radiation within the first 10 μm , the thin sample is partly penetrated, and therefore cannot absorb all incoming power. In this regard, the thick silicon has a larger metal-like layer, which reflects incoming THz radiation, resulting in a lower transmission. The thinner silicon sample is used for transient metamaterial generation, because of its homogeneous excitation profile. Whereas the 375 μm Si has a Lambert-Beer-type intensity absorption, the thin silicon has multiple reflections at its backside, leading to more homogeneous pumping, which is beneficial for metamaterial generation. While these reflections also happen in the thick samples, the comparatively long optical way leads to a long separation in the time, wherefore these reflections are only considered in the pumped area.

Compared to Silicon, GaAs has the highest transmission decrease per incoming pump fluence. Two opposing effects occur: GaAs is a direct semiconductor, and therefore the generation of charge carriers is an order higher, which according to the Drude model leads to an even stronger decrease

in the dielectric function. At the same time the absorption depth is only $1\mu\text{m}$, leading to a smaller excited region. Therefore, the carrier density is larger than in Silicon.

Modeling

For a deeper understanding, the pump-dependent transmission for samples is modeled with the Fresnel transmission formulae and comprehensively explained in appendix A.2. The modeling-parameter is the amount of free charge carriers N , which according to formula 2.10, modifies the refractive index and therefore the transmission. While the thin silicon sample can be considered as one homogeneous illuminated layer, the thicker Si has to be treated as two-layer systems with one excited and one unexcited layer. The estimated transmission for thin/thick Silicon resembled the experimental data in good approximation, thus it is possible to extract the amount of charge carriers per pump fluence. The results are depicted in figure 4.4. In (a) the plasma frequency ω_p is plotted against the fluence. As can be seen the plasma frequency increases proportional to the square root of the pump fluence, which was predicated by eq. 2.11. While only a part of the pump beam is absorbed within the thin Si sample, all of the pump is absorbed in the thicker Si, leading to a higher plasma frequencies. In figure 4.4(b) the square plasma frequency indicates the linear response of the dielectric function to increasing fluence. GaAs can be modeled analogous, and was therefore considered separately.

Dependence on pump-probe delay

After verifying pump-dependence on the transient structures, the dynamic behavior has to be characterized. A THz pulse needs roughly 0.6-4 ps to traverse the sample (depending on thickness). In this time, the induced refractive index change has to remain undamped. To validate this, the delay between optical pump and THz probe is varied, while the pump fluence is kept 0.7 mJ/cm^2 . Figure 4.5(a)/(b) shows the dynamical change in transmitted electric field after photo-excitation of Si and GaAs, respectively. The plot shows the time delay between incoming THz radiation and optical pump and the peak-to-peak amplitude of the transmitted THz transients. For negative pump delays the optical pump pulse arrives after the THz probe pulse, and as a result the EOS signal is equal to the absence of any photo-excitation. For $\tau > 0$ the charge carriers need roughly 0.1 ps for Si and 0.7 ps for GaAs to thermalize, and therefore minimize the EOS-signal amplitude. As can be seen, the reduced THz electric field amplitude remains for tens of ps.

With this result, it is proven that photo-generated refractive index changes enable a controlled ps switching of semiconductors from transmissive to absorptive behavior that last long enough to modulate a whole THz probe pulse. Therefore, in subsequent measurements, pump-probe delay is set to approximately 10 ps.

4. Results and discussion

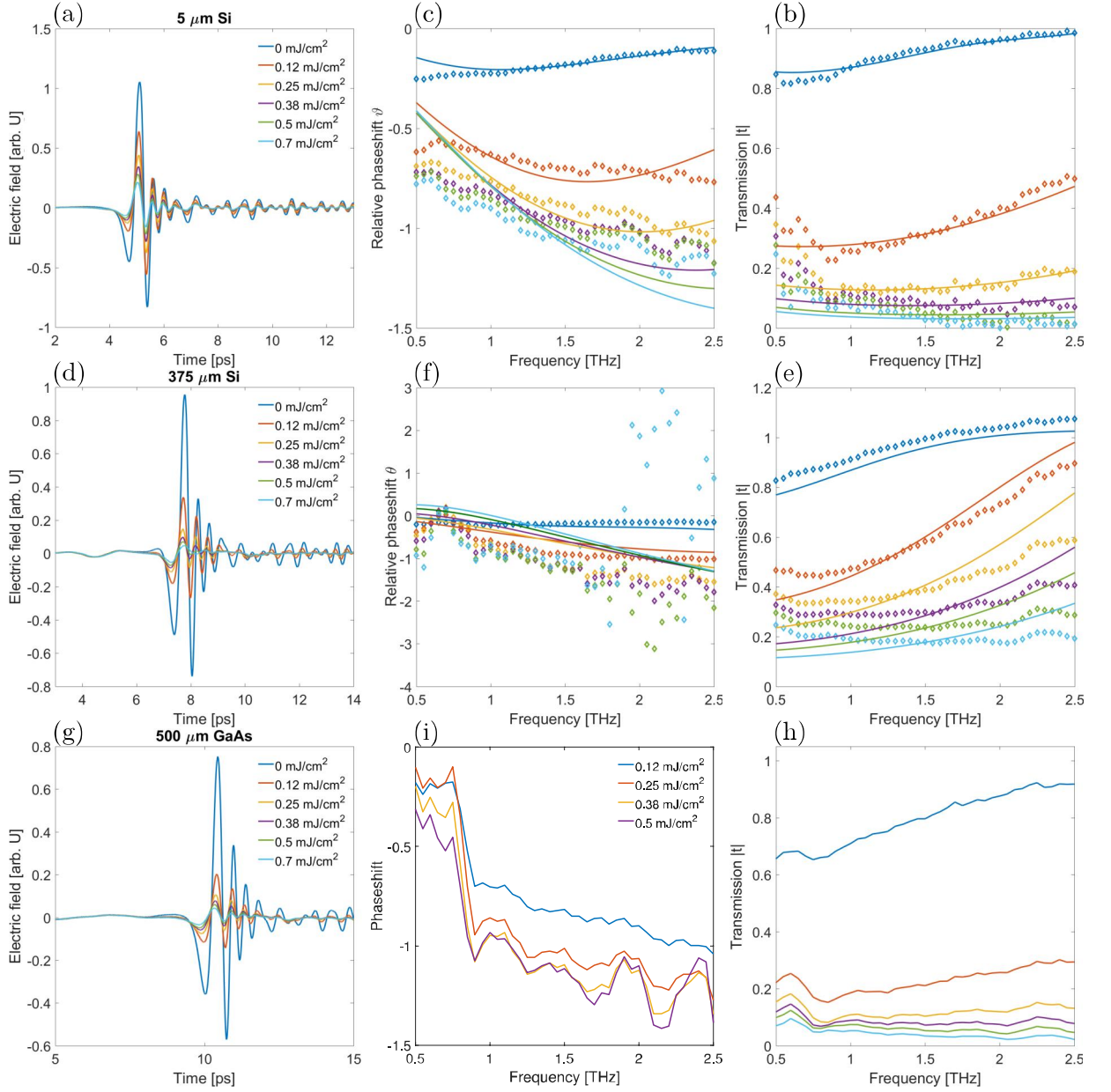


Figure 4.3.: Electric field, phase delay and spectral intensity: A 5 μm Silicon sample (a)/(b)/(c), a 375 μm silicon sample (d)/(e)/(f) and a 500 μm GaAs sample (g)/(h)/(i) are measured in transmission with the THz-TDS as before. Figures (a),(d) and (g) show the measured electric field, figures (b),(e) and (h) show the spectra acquired through Fourier transformation of the corresponding fields normalized to the unexcited spectra and figures (c),(f) and (i) show the phase shift of the transmitted THz wave referenced to the unexcited samples. While the dark blue curves indicate the absence of any photo-excitation, the red, brown, violet, green and cyan colored curves show transients for incident pump fluences of 0.12, 0.25, 0.38, 0.5, 0.7 mJ/cm², respectively. High fluences induce more electron-hole pairs, resulting in metal-like behavior of the semiconductors viz. reduced THz transmission.

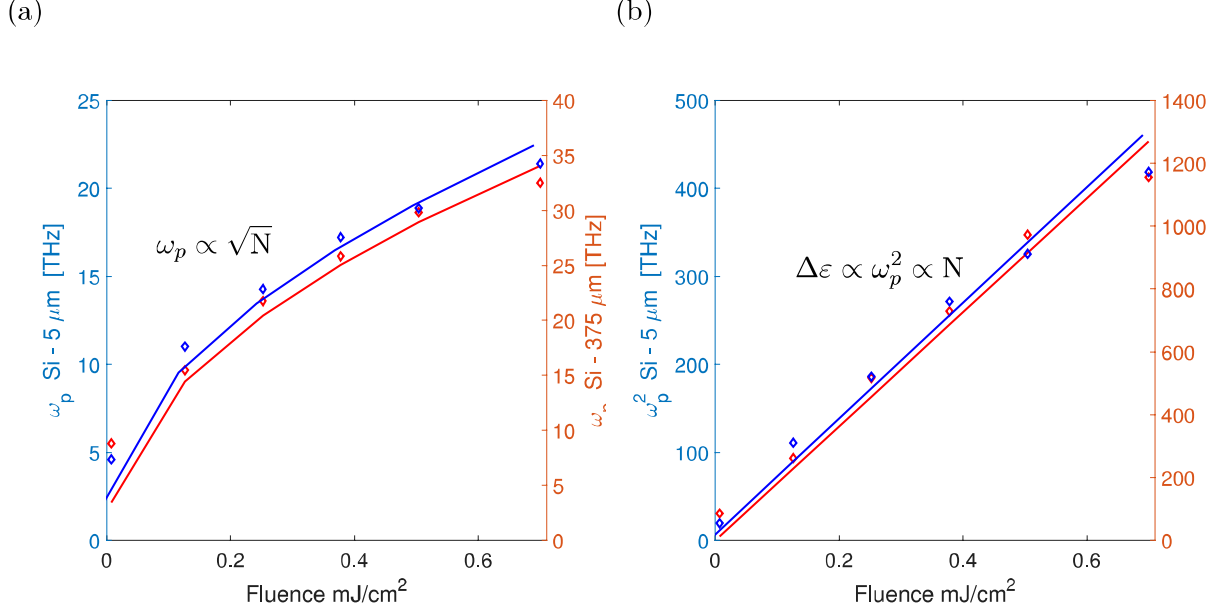


Figure 4.4.: Plasma frequency for various pump fluences: This figure shows the plasma frequency ω_p for Silicon, which was acquired by fitting the experimental transmission with the Drude model for varying pump fluences. The generation rate for GaAs is roughly an order higher, because GaAs is a direct semiconductor. The diamonds show the calculated plasma frequency, while the line shows the expected square root fluence dependency.

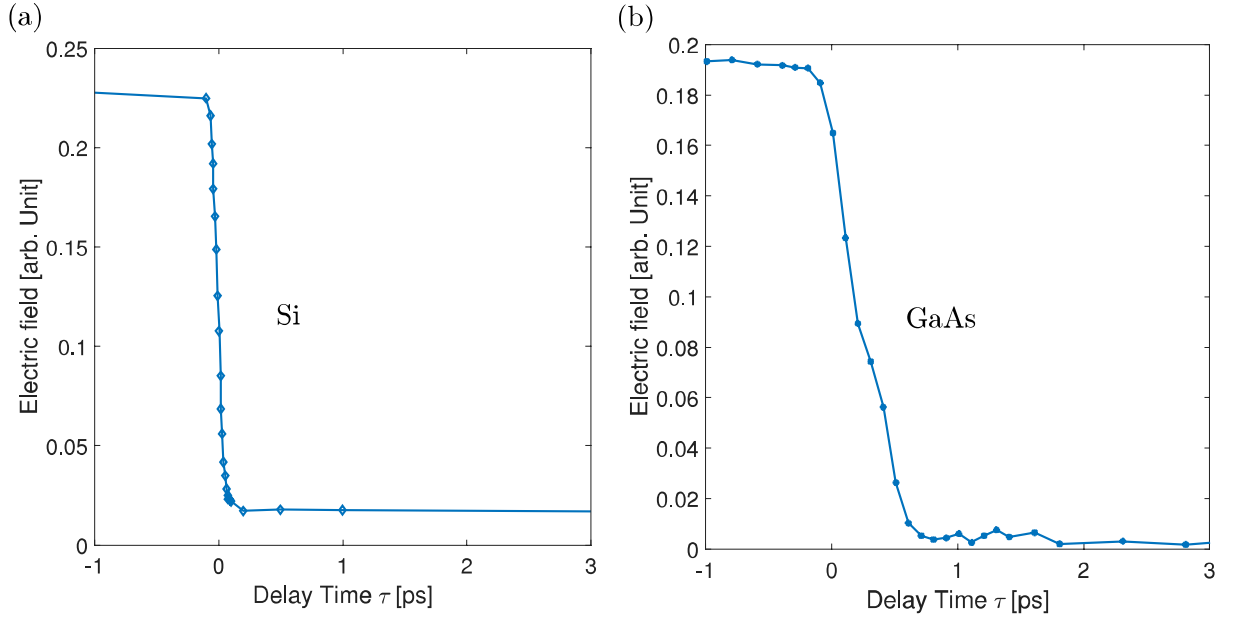


Figure 4.5.: Electric field for pump-probe delay: Dynamic behavior of the photo-excited electron-hole-pairs in Si (a) and GaAs (b). At a pump fluence of $0.7 \text{ mJ}/\text{cm}^2$ the delay between optical pump and THz probe is varied. The vertical axis shows the peak-to-peak amplitude of the transmitted THz transients. For negative pump delays the optical pump pulse arrives after the THz probe pulse. For $\tau > 0$ the charge carriers need a short time to thermalize and therefore minimize the signal amplitude.

4.3. Wire grid THz polarizer

Time-domain Data

After validating the foundations for transient THz metamaterials, evaluation of applications for THz metamaterials is enabled. In this section subwavelength wire-grid polarizers are examined. As shown in figure 4.6(a), the SLM imprints a grating profile (Period $\Lambda = 32\mu\text{m}$, metal fill factor $f = 3/8$) onto the pump beam cross section, which is then translated into an electron-hole plasma in the semiconductor. To control the quality of the projected grid, a CCD camera is placed at the sample position.

The samples are again measured with the TDS setup, and the transmitted electric field contains the optical information, which are extracted when compared to a reference signal (unexcited sample). Besides fluence and size, the wire grid polarizer are also tested for different incident polarizations, but instead of rotating the incoming electric field, rotation of the imprinted pattern by 90° is done via SLM. The wire grid of choice has a unit cell of $\Lambda = 32\mu\text{m}$, while the gap between to wires has a size of $20\mu\text{m}$. In the previous experiment high fluence proved to induce the greatest change in refraction, and therefore the pump fluence is set to 0.7 mJ/cm^2 . The delay between optical pump and THz probe is set to 10 ps.

In the first measurement, the transmitted electric field for polarization parallel (\parallel) and perpendicular (\perp) to the wires is measured. The results are displayed in figure 4.6(c). As expected, the unexcited sample shows the highest electric field amplitude. The transmitted THz transient of the perpendicular wires is roughly 0.3 times weaker than the reference amplitude, which is expected, because 5/8 of the unit cell are illuminated and therefore highly reflective/absorptive for THz radiation. However compared to the parallel wire configuration, which has the same illuminated fraction of the unit cell, the transmitted \perp THz signal is 3 times larger, illustrating the anisotropic behavior of the transient grid and demonstrating its filtering capabilities.

Fourier domain

To gain further insight into the frequency dependent transmission properties, the electric fields are Fourier transformed and the transmission is calculated according to eq. 4.1. The transmission for both polarizations is presented in 4.7(a). At any point in the selected frequency window, the perpendicular transmission is greater than the parallel transmission. But while the \parallel transmission is only monotonically increasing with frequency, the \perp counterpart has a broad maximum at around 2 THz. The lower frequency components are again more noisy, because of the weaker spectral intensities.

When looking at the phase of the complex transmission, one can extract the phase (shift) information, which is shown in fig. 4.7(b). Notably, the parallel wire-grid exhibits a larger negative phase shift, which implies more metal-like behaviour than the perpendicular component.

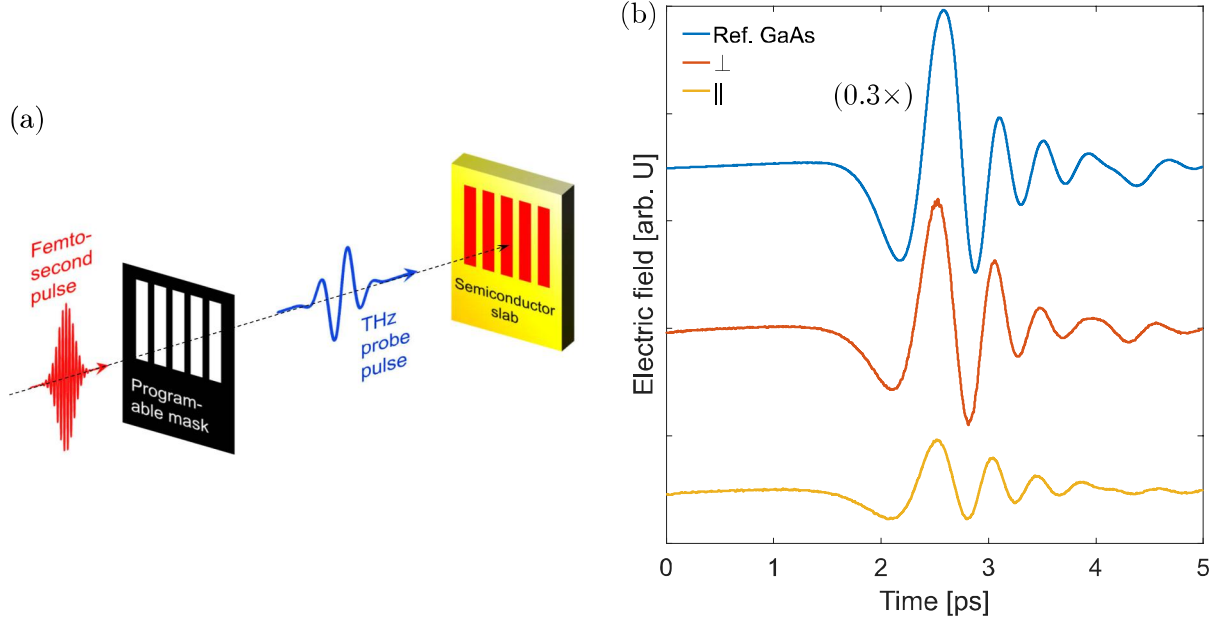


Figure 4.6.: Time-domain data wire grid polarizers: (a) Scheme of a transient WGP induced by femtosecond grayscale lithography. An 800 nm femtosecond laser pulse with a homogeneous beam cross section generates an electron-hole plasma with a spatially varying density in a semiconductor slab, thereby inducing a refractive-index modulation ranging from metallic to dielectric. (b) Time-domain characterization of GaAs without excitation and with transient wire-grid polarizer perpendicular and parallel to the THz polarization. The difference in amplitude of the waveforms are a clear signature of the anisotropic response of the transient metamaterial.

Fluence dependency

In the next measurements a 5 μm Silicon sample is used, because of its homogeneous absorption profile. For determining the fluence dependence, analogous measurements as for homogeneous excitation were done for WGPs. The resulting transmissions for \parallel and \perp are shown in figure 4.8(a)/(b), respectively. Both polarizations show a decrease in transmission for fluence increase due to metal-like behavior. In contrast to the constant transmission for \perp orientation, the \parallel transmission increases for higher frequencies. Shorter wavelengths approach the stripe size, therefore the wire-grids lose their filtering abilities. This behavior becomes even clearer when looking at the relative transmission, which is t_{\parallel}/t_{\perp} and is depicted in 4.9(a).

As can be seen, the relative transmission increases with frequency. The transmitted \parallel and \perp electric fields become more alike. The integrated transmittance is shown in figure 4.9(b), showing a decrease with increase in fluence. A stronger optical pump increased quality of the transient filter.

Dependence on wire size

The influence of wire/gap size on transmission is examined. Therefore the optical pump (0.7 mJ/cm^2) and period ($\Lambda = 32 \mu\text{m}$) remain constant, while the SLM generates varying gap sizes

4. Results and discussion

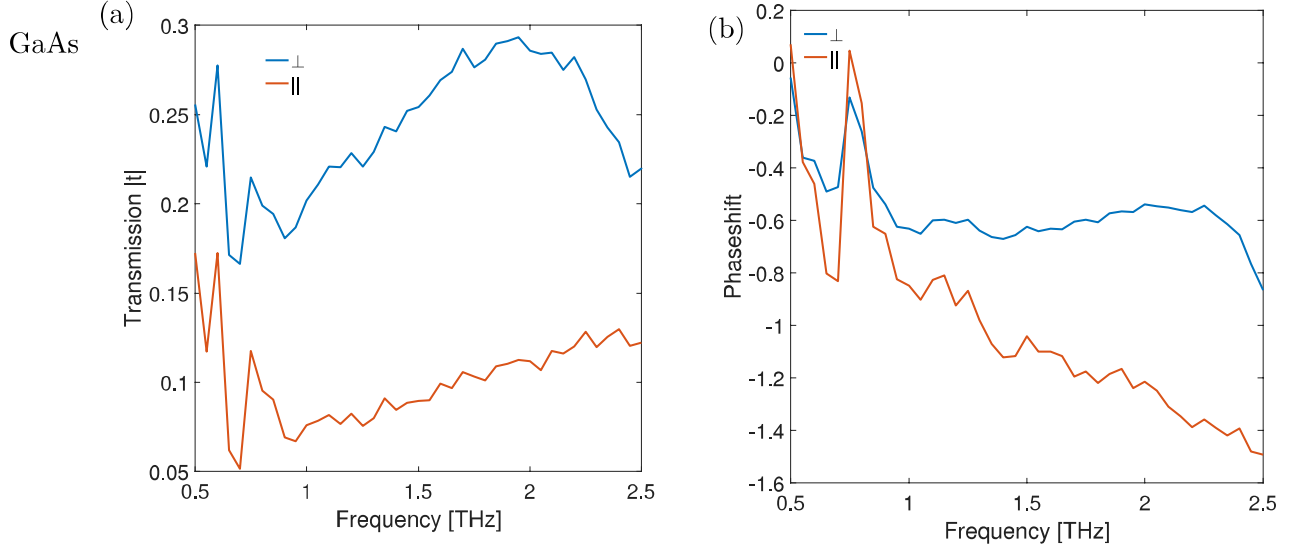


Figure 4.7.: Transmittance of the transient wire-grid polarizer: (a) Transmission of the GaAs slab 10 ps after excitation with the pump pattern of figure 4.6, referenced to the unexcited slab. The spectra demonstrate that the transient structure acts as a polarizer. (b) Spectral phase shift, revealing the more metallic behavior (negative phase shift) of the structure for THz radiation polarized parallel to the transient wires.

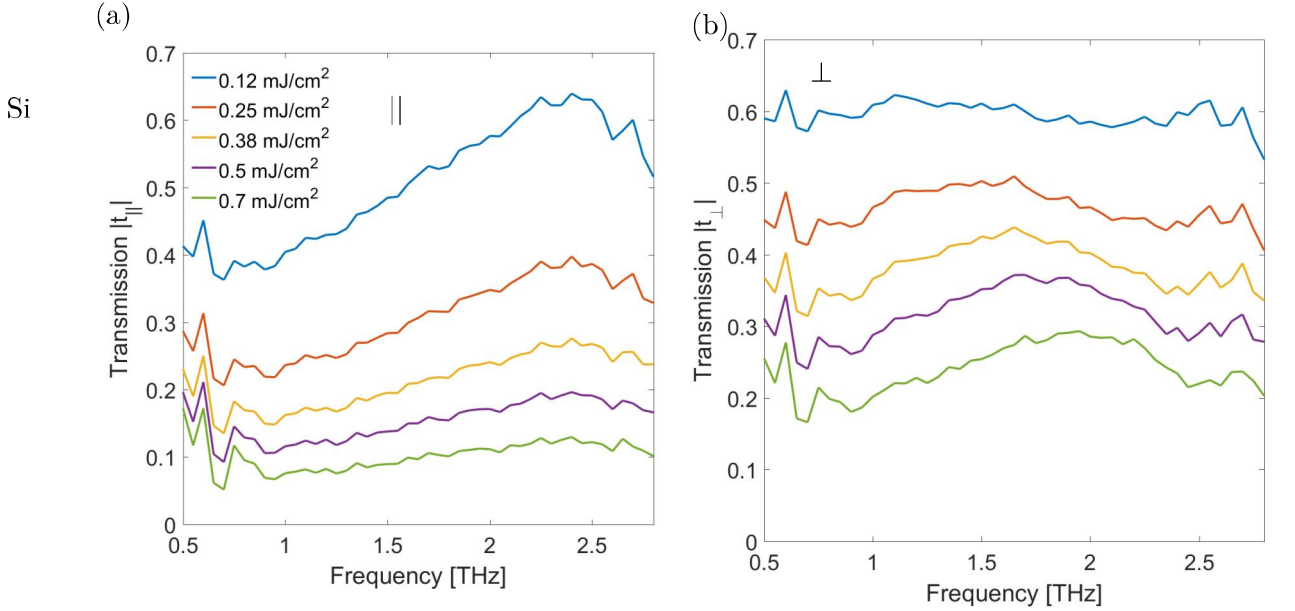


Figure 4.8.: Pump dependency WGP transmission: (a) and (b) show the transmission of parallel and perpendicular, respectively compared to the unexcited Si slab. While the perpendicular transmission remains relatively constant over the frequency domain, the parallel transmission increases with higher frequency, proving the less effective sub-wavelength characteristics.

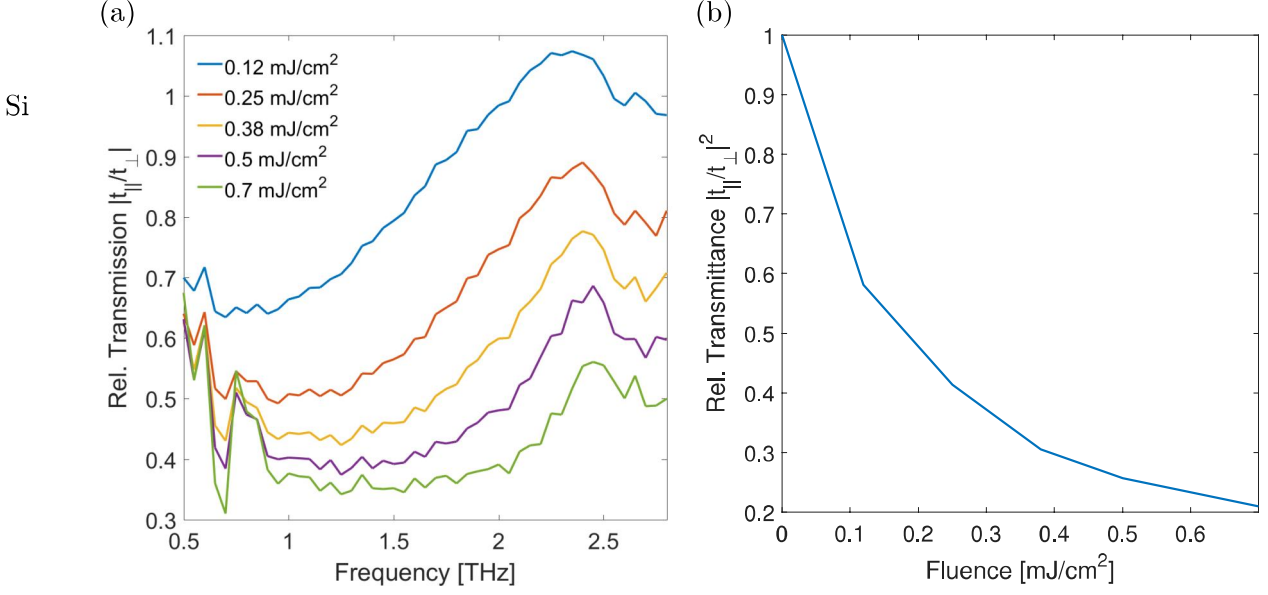


Figure 4.9.: WGP performance: Figure (a) shows the relative transmission $\tilde{t}_{||}/\tilde{t}_{\perp}$ of 5 μm Si for various pump fluences comparing the pumped parallel to perpendicular wire-grid pattern. The WGPs become better (higher extinction ratio) for large carrier densities. (b) shows the integrated relative spectral transmission, which relates the parallel and perpendicular polarizations transmission, therefore indicating the filtering capabilities of a polarizer.

from 8 to 28 μm . Measurements are done analogous to before. The absolute transmission for $||$ and \perp wires is shown in figure 4.10(a)/(b), respectively. An increase in gap size leads to an higher transmission, which is trivial, because an increased gap means less illumination. The ($||$) transmission rises faster for increasing gap sizes. For the gap sizes 20-28 μm , the \perp transmission increases nearly linear with the frequency, while for gap sizes 8-16 μm the behavior is comparable to the $||$ transmission, but weaker.

The interplay between both polarizations in the relative transmission is shown in figure 4.10(a). While small gaps show only weak frequency dependency in transmission, broad gaps exhibit a stronger filtering, due to a strongly illuminated sample. Therefore, a trade-off between filtering quality, transmission and frequency dependence exists.

Plotting the integrated relative transmission, as depicted in figure 4.11, shows the optimal gap, which is 20 μm . An increase/decrease in gap size decreases the filtering quality of the wire grids, which can be accorded to an increased mismatch between wavelength and wire size.

With the evaluation of gap size and fluence, the best working wire-grid could be determined. A 32 μm unit cell with a gap size of 20 μm with high fluence delivers the best filtering capabilities for electric field between 0.5 and 2.5 THz. For higher or lower frequencies the periodicity and stripe width have to be rescaled accordingly.

4. Results and discussion

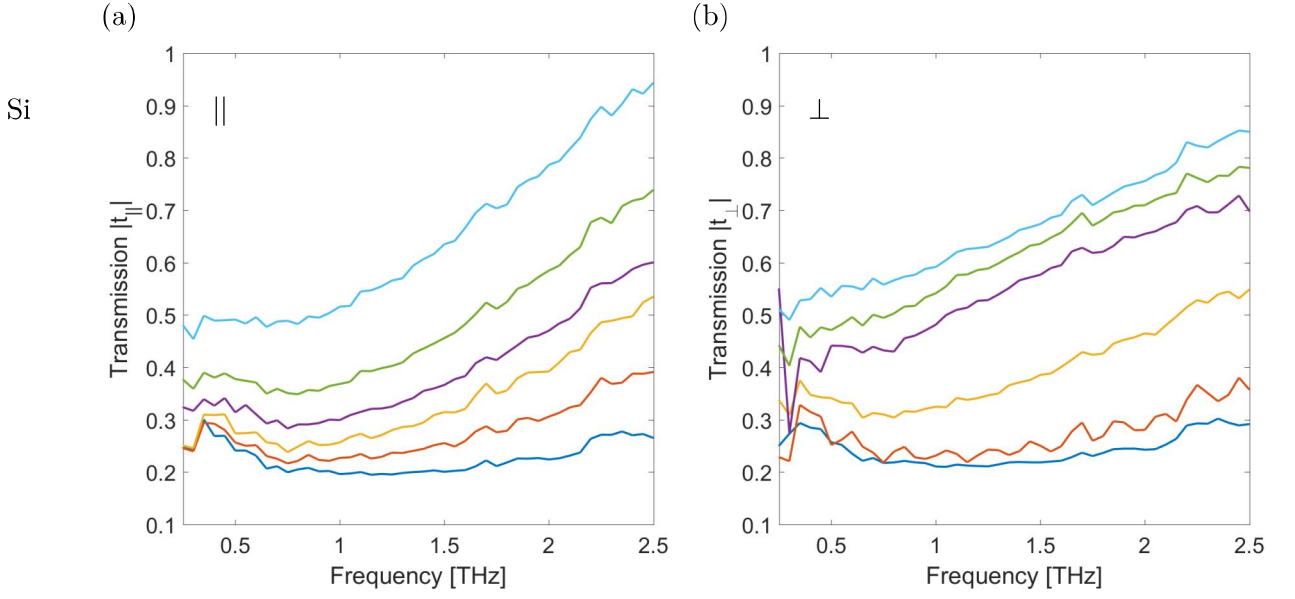


Figure 4.10.: Transmission for varying wire sizes: (a) and (b) show the transmission of parallel and perpendicular wires, respectively compared to the unexcited Si slab. 20 μm gaps exhibit the least rel. transmission. Narrowing and broadening increases relative transmission, therefore decreasing the filtering.

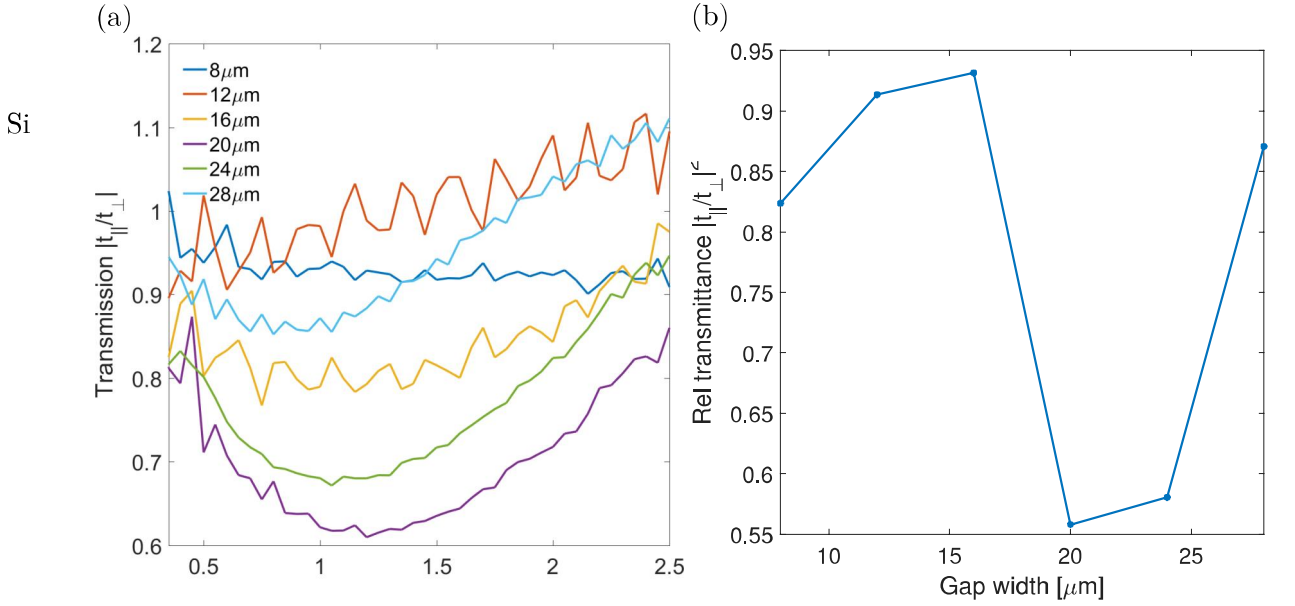


Figure 4.11.: Stripe size dependency on relative transmission: (a) shows the relative transmission $|t_{||}/t_{\perp}|$ of 5 μm Si for various wire widths, while keeping the period $\Lambda=32 \mu\text{m}$ constant, comparing the pumped parallel to the perpendicular wire-grid pattern. 20 μm exhibit the strongest extinction, while narrowing and broadening decreases the filtering. (b) The recorded relative transmission between a parallel and a perpendicular wire grid with a fixed period of 32 μm , while the pump fluence is kept at 0.7 mJ/cm^2 is presented for various gap sizes. The filtering quality has its maximum at 20 μm gap size and decreases for smaller and wider gaps.

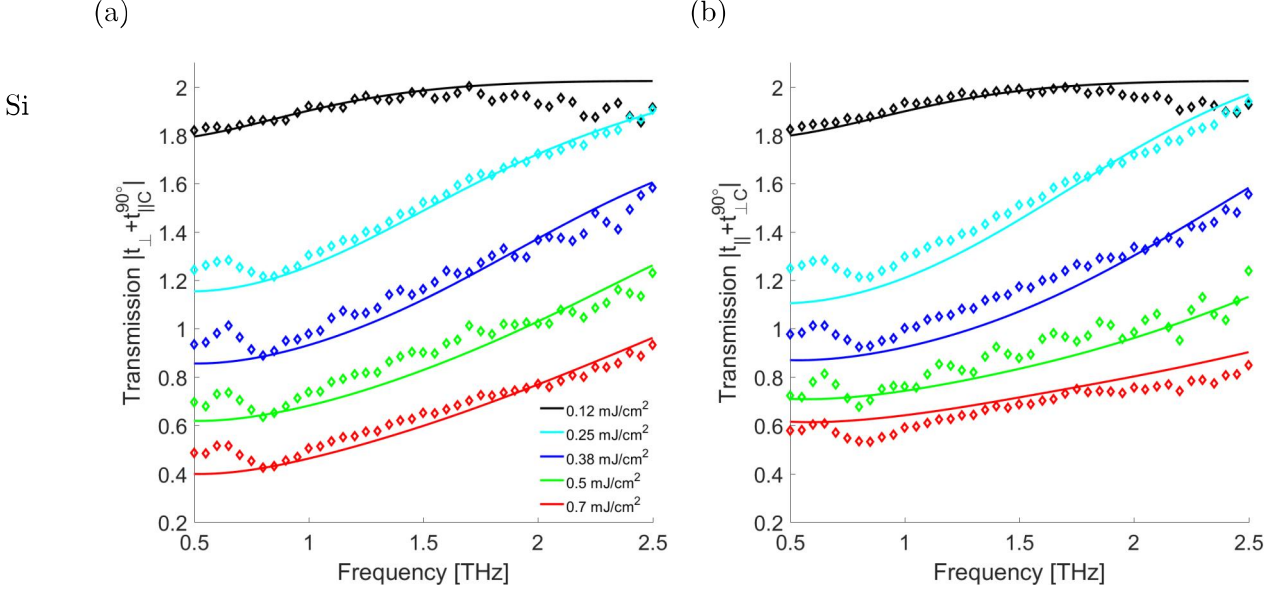


Figure 4.12.: Testing Babinet's principle: This figure shows the sum of the electric field transmission of a transient WGP with a period of $32 \mu\text{m}$ and a gap size of $20 \mu\text{m}$ and its complementary structures, i.e. $32 \mu\text{m}$ period, a gap size $12 \mu\text{m}$, under varying pump fluences. (a) shows $|t_{\perp} + t_{\parallel}^{90^\circ}|$ and (b) depicts $|t_{\parallel} + t_{\perp}^{90^\circ}|$. The experimental data (points) are approximated with Fresnel transmission formulae (solid lines), considering the Drude model and the WGP pump profile.

Babinet's principle

After determining the best working transient wire-grid polarizer, the validation of the Babinet's principle for this metastructure shall be tested. The principle describes the relation between a structure and its complementary structure, which in case of wire-grids means gap and stripe size are switched. For more detailed information see section 2.1.2. The Babinet's theorem states that the transmission of a structure and its complementary structure illuminated by a complementary field, i.e. 90° rotated polarization, sum up to the transmission of no structure. This is only valid for infinitely thin and perfectly conducting screens. Compared to the wavelength $\lambda_{1 \text{ THz}} = 300 \mu\text{m}$, the $5 \mu\text{m}$ silicon is relatively thin, fulfilling this part of the condition. In this experiment the perfectly conducting condition shall now be validated. Therefore the semiconductors are pumped with various fluences, increasing their conductivity, to determine at which point, the perfectly conducting condition can be considered as valid. Because THz-TDS cannot compare transmission through photo-excited structures and air simultaneously, this thesis modulates the Babinet's principle by comparing structure and complementary structure with the transmission through unexcited sample.

With the Drude model and the transfer matrix method, the experimental data from section 4.2 and the WGP intensity profile (cf 4.6(b)), the theoretical transmission values for the Babinet's principle have been compared to the experimental data. The results are shown in figure 4.12(a)/(b) for $|t_{\perp} + t_{\parallel}^{90^\circ}|$ and $|t_{\parallel} + t_{\perp}^{90^\circ}|$, respectively.

As can be seen the theoretical calculations (line) are in a good approximation to the experimental results (points). The overall transmission decreases, as expected, with an increase in pump fluence.

4. Results and discussion

The 5 μm silicon is expected to have a roughly constant absolute transmission. In the characterization of the unexcited samples (see section 4.1) this transmission was determined as 0.8, which the sum of structure and complementary should share. Considering the shape of the transmission curves, an increase in fluence leads to a flattening of the curves. However the transmission value of $|t_{\perp} + t_{||C}^{90^{\circ}}|$ and $|t_{||} + t_{\perp C}^{90^{\circ}}|$ for the highest fluence are roughly between 0.4-0.8 and 0.5-0.8, respectively. Considering the former mentioned problems in the fitting of the Drude model to the thin sample, probably due to induced lensing, these values seem a good approximation. The transmission is expected to flatten even further for higher frequencies, but with the results presented here, the Babinet theorem is already well fulfilled.

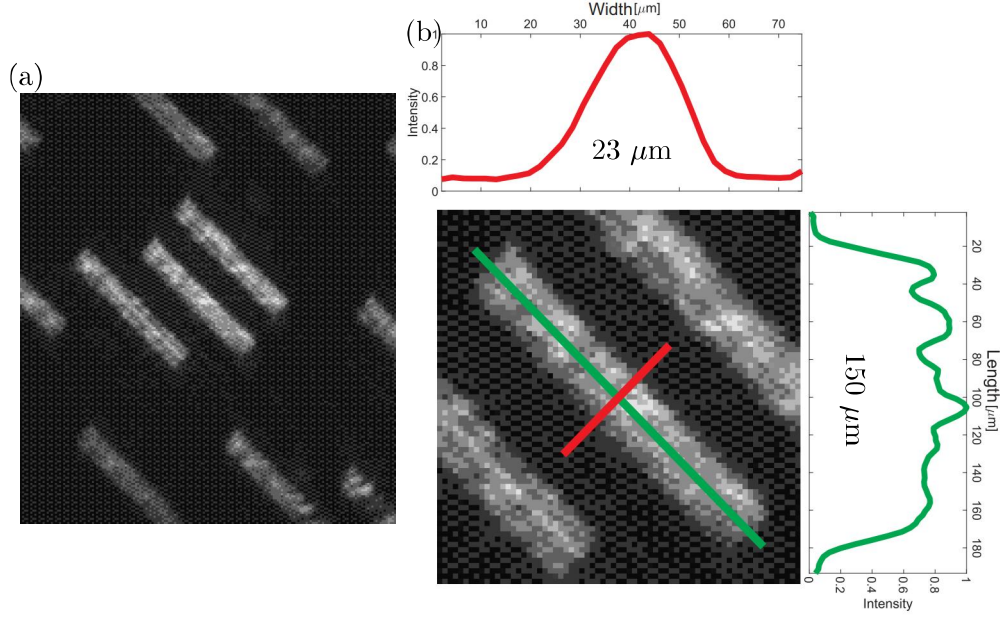


Figure 4.13.: Dimensions dipole antennas: (a) Measured intensity image of an array of photo-generated THz antennas. (b) Detailed view of a single rod. The upper and right plots are the intensity profiles along the horizontal and vertical dotted lines. The vertical axis and the color scale indicate the pump fluence of mJ/cm^2 . The FWHM of this intensity profiles mark the dimension of the rods.

4.4. THz dipole antennas

After establishing transient polarizer based on simple wire grid, which are one-dimensional structures, more complex 2D periodic dipole antennas are examined. The rods antennas are expected to induce broadband THz resonances leading to local field enhancement in the sample, which could be beneficial for many applications.

As in the previous experiment, the imaged patterns are characterized before the THz-TDS measurements. Again the CCD camera is placed in the sample position and an intensity picture is recorded. One of the acquired rod arrays is shown in figure 4.13(a). A single linear antenna is shown in fig 4.13(b). The effective size of this antenna is defined by the FWHM of its intensity profile: its dimension are $23 \times 150 \mu\text{m}$. Afterwards the camera is replaced by $5 \mu\text{m}$ Silicon.

For the THz transmission measurements, the sample was illuminated with an optical pump pulse photo-generating the antenna structures. The transmitted electric field was measured and compared to the unexcited sample transmission. The time delay between pump and probe was set to 10 ps. The THz transmission was obtained through Fourier transformation of the electric field.

The first measurement examines the influence of the rod width on the transmission in the frequency domain. Because later on the Babinet's principle will be examined, all experiment are done for structure and complementary structure. The complementary structure to a rod antenna is a slit antenna.

Figure 4.14 shows the transmission spectra of photo-generated THz slits fig. 4.14(a) and antennas fig. 4.14(b) with 32 and $64 \mu\text{m}$ width, $232 \mu\text{m}$ length and $352 \mu\text{m}$ pitch. In contrast to the

4. Results and discussion

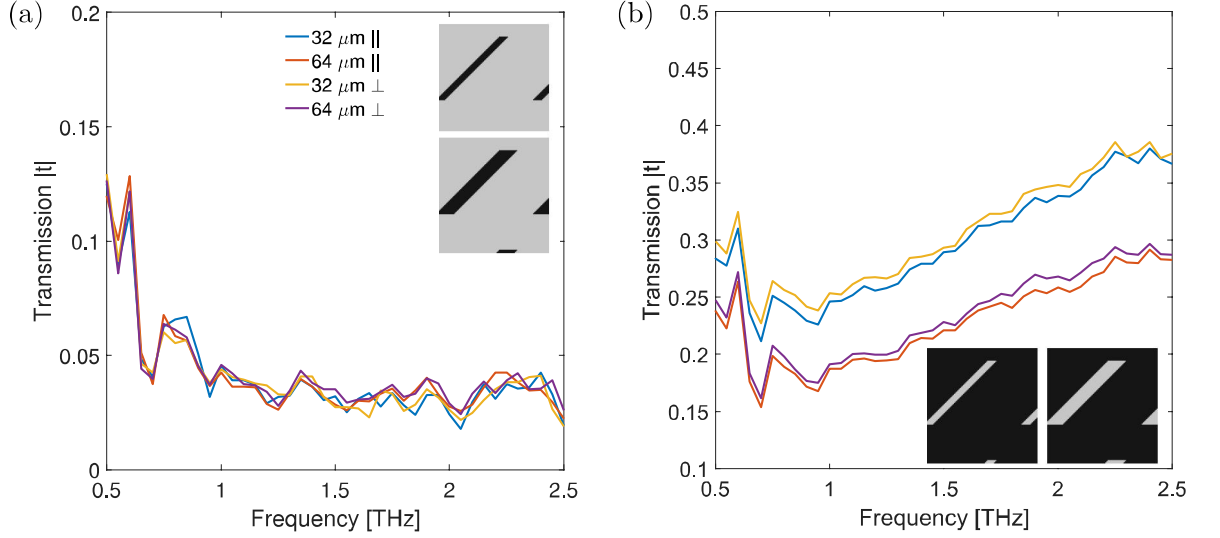


Figure 4.14.: Antenna transmission - width variation: Transmission spectra of photo-generated THz antennas on a $5\ \mu\text{m}$ layer of Silicon. The length of the rods $232\ \mu\text{m}$ and period $346\ \mu\text{m}$ are fixed, while the width is varied from 32 to $64\ \mu\text{m}$. (a) Pumping everything but the rods, induces slit-antennas. The width of the slits is doubled, while the transmission remains unchanged. (b) Only the rods are excited, turning them into THz antennas. Broadening leads to an increase in transmission and peak-to-peak signal, probably due to resonant behavior. The polarization of the incident wave proves negligible.

expectation of an anisotropic structure, that a rod certainly is, the transmitted electric field was independent of the polarization of the THz beam. This behavior is currently not understood. All further measurements were done with the polarization set parallel to the long axis of the rods.

When the sample is illuminated with slit antennas (cf. 4.14(a)) most of the surface is fully excited. Therefore the weak transmission in the experiment is expected. Furthermore, the width variation seems negligible, probably because the strongly pumped sample dampens most of the resonances. Generation of antennas (see fig. 4.14(b)) results in a stronger transmitted electric field. For high frequencies an increased transmission can be seen. This increase is most likely due to the frequency influence in the Drude modulation. Furthermore, transmission increases for expanded rods. A larger pumped area should lead to decreased amplitude, while in this counterintuitive case, the signal increases, indicating resonant excitation in the thinner rods, probably due to local field enhancement.

Varying pitch

In the next experiment, the rod dimensions are fixed, but the distance between rods is varied. With this, any grid-type resonances are examined. The transmitted electric fields are measured for $340\ \mu\text{m}$, $400\ \mu\text{m}$, $456\ \mu\text{m}$, $568\ \mu\text{m}$ and $636\ \mu\text{m}$ distances between the rod, and Fourier transformed to access the spectral information. The resulting transmission spectra are shown in figure 4.15.

Pumping the slit antennas (cf. 4.15(a)) shows constant transmission, which is unaffected by a variation of periodicity. The initial increase is most likely due to increased noise, while the constant

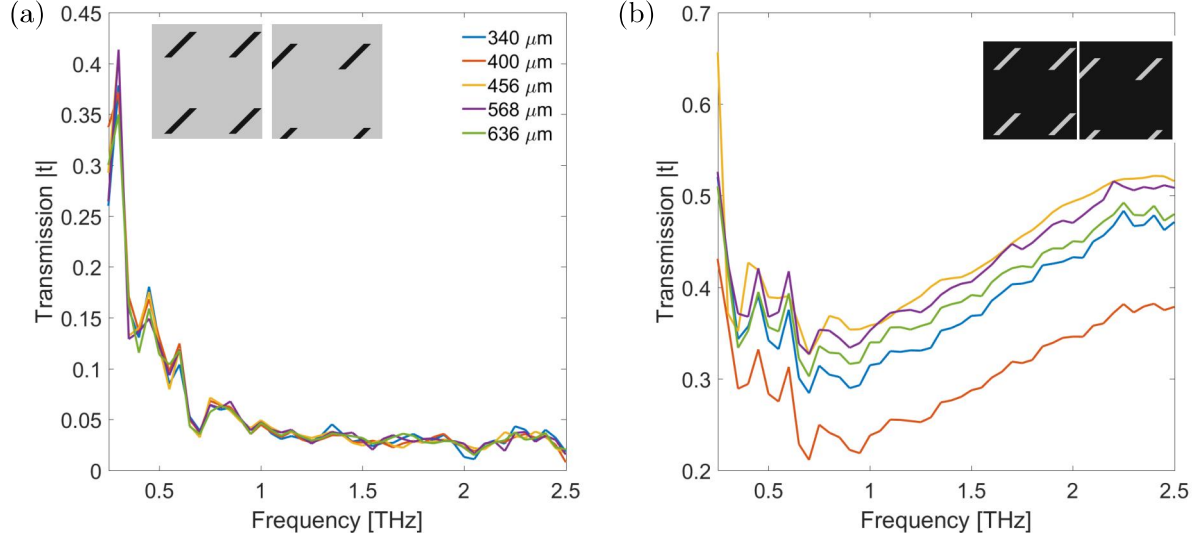


Figure 4.15.: Pitch dependency transmission: Transmission of THz antennas on a 5 μm layer of Silicon. The length of the rods 232 μm and their width 64 μm are fixed, while the distance between rods is varied. (a) When pumping the slit antennas, an initial increase in transmission is followed by a constant function. The extinction seems to be unaffected by the slits pitch. (b) Pumping the rods gives rise to a resonance at 0.7 THz, whose maximum occurs at periodicity of 400 μm , probably due to grid-type resonances.

is based on the nearly homogeneous photo-excitation, suppressing most of the THz transmission. The antenna counterpart (b) has a broad drop of transmission at 0.7 THz, which indicates a resonance. For higher frequencies the transmission rises, probably because the antennas become off-resonant combined with the typical Drude frequency dependency. The overall minimum in transmission occurs at a distance of 400 μm between the antennas, which could be due to grating-type resonances ($\Lambda \approx \lambda$).

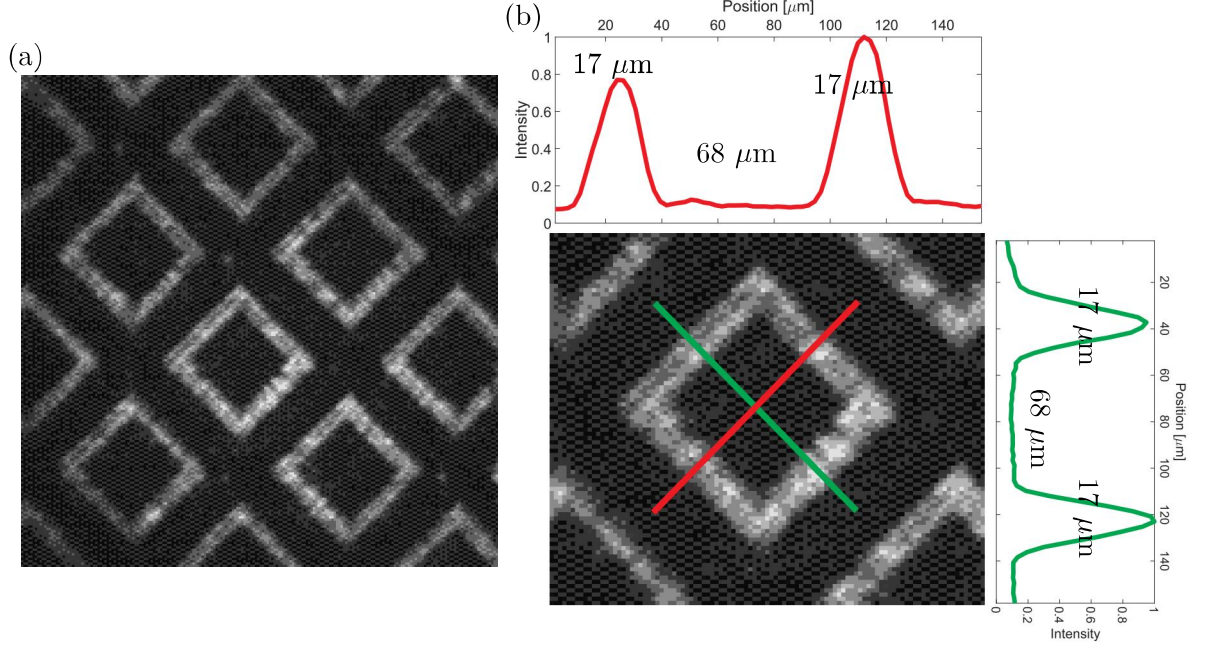


Figure 4.16.: Dimensions metamaterial: (a) Image of an array of photo-generated THz bandpass filters. (b) Close view image of a rectangular filter structure. The upper and right plots are the intensity profiles recorded by a CCD camera along the green and red colored lines. The dimensions of the filters are defined by the FWHM of the pump beam intensity.

4.5. Outlook: Metamaterial for local field enhancement

After demonstrating polarization/broadband frequency filters via wire grids and dipole antennas, high-pass filter are investigated. Therefore, more complex structures like (split) ring resonators, hole arrays, crossed wires and various combinations of the former are utilized, complicating theoretical predications. While rudimentary descriptions and simple equivalent circuit models exist, the only provide rough orientation for the dielectric function of the metamaterial. Current studies mostly rely on established shapes and materials, which do not exist for photo-generated metamaterials, yet. Therefore the last experimental chapter of this thesis, investigates a high-pass metamaterial. For a first approach, the parameter space is minimized by selecting a rectangle ring with a rectangular filling structure. Figure 4.16(a) shows an intensity profile of these metastructures, while the FWHM is evaluated with the plot profile, shown in (b), to determine its dimensions. Its size is $143 \mu\text{m}$, width $17 \mu\text{m}$, while the inner gap has a span of $68 \mu\text{m}$. To exclude polarization effects, the unit cell is kept symmetric regarding perpendicular and parallel electric field. The intensity mask is projected onto a $5 \mu\text{m}$ Silicon wafer. The transmitted THz transient is measured, comparing excited and unexcited Silicon via a chopped imaging beam. The electric field is Fourier transformed and the transmission is calculated (eq. 4.1). The absolute transmission regarding frequency variation is shown in figure 4.17.

While frequencies greater than 1 THz and lower than 0.5 THz show an increased transmission, the gap shows a lower ratio. This frequency interval could contain resonances, which result in a local enhancement of the electric field within the structure, leading to a higher absorption ratio. In fab-

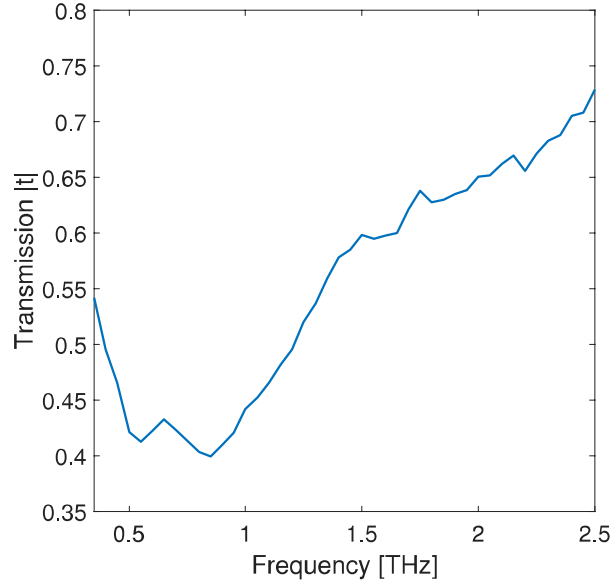


Figure 4.17.: High-pass resonances in transmission: Absolute value of the transmission ratio of 5 μm Silicon unexcited and excited with the pattern in figure 4.16 regarding frequency variation. The decrease between 0.5 and 1 THz could be an indicator for resonances within the photo-generated THz metamaterial.

ricated, non-transient, metamaterials, these resonances are typically narrower, but the scattering of excited free charge carriers smears out these resonances resulting in broader responses. However the spectral range of the increased absorption is narrow compared to the antenna behavior of the former section.

This first explorativ attempt to create a high-pass metamaterial shows promising results, while being far from optimized. Further parameter scans (pump fluency, pattern size/widths, sample) could pave the way to full understanding of the activation and shape of resonances in transient metamaterials.

Conclusion

In this thesis, a setup for the ultrafast generation and characterization of sub-wavelength terahertz photonic structures was established and tested. The structures were generated by illuminating a semiconductor slab with a femtosecond laser pulse whose beam cross section is intensity-modulated with a suitable spatial profile. Illumination of the semiconductor induced a refractive-index landscape whose shape can flexibly be defined with a pixel size of $4\ \mu\text{m} \times 4\ \mu\text{m}$ by using a programmable spatial light modulator. Amplitude and phase of the transmission of the photo-induced metamaterials were measured by terahertz time-domain spectroscopy from ≈ 0.5 to $2.5\ \text{THz}$.

In the course of building the setup, the spatial light modulator was installed and characterized. An intensity modulation-depth exceeding 99% was achieved and enabled the generation of beam patterns with high contrast. Measurement of the point spread function and calculation of a two-dimensional -cross- correlation ensured precise imaging.

Time-resolved time-domain spectroscopy of unexcited semiconductors was used to determine the optical constants of the transient structures, their fluence dependence and dynamics. The resulting complex-valued transmission spectra were modeled using a combination of the Drude model, Fresnel formulae and effective medium theory.

To test the setup, wire-grid polarizers, arrays of rod antennas and rings were realized first. The transient wire grid polarizers achieved a power extinction ratio on the order of 10. Using these structures, I also investigated the validity range of the Babinet's principle. It was found, that Babinet's principle is better fulfilled the more metallic the induced structures are. Gallium arsenide and Silicon (which exhibit a pump penetration depth of ≈ 1 and $10\ \mu\text{m}$) were observed to deliver similar results.

The rod antennas were shown to allow broadband high pass frequency filtering, while rectangular ring-based metamaterials, could induce narrow-band resonances, which are possibly accompanied by locally enhanced THz fields. Both structures provided power extinction on the order of 6.

In future studies, transient metamaterials will permit the construction of switches: filters can be switched on within $\approx 100\ \text{fs}$, thereby allowing modulation of a terahertz pulse that is just traversing the semiconductor slab.

German Summary / Deutsche Zusammenfassung

In dieser Masterarbeit wurde ein experimenteller Aufbau für die ultra-schnelle Erzeugung und Charakterisierung von photonischen Terahertz-Strukturen, die kleiner als die Wellenlänge sind, aufgebaut und getestet. Die Strukturen wurden durch Beleuchten eines Halbleiters mit einem Femtosekunden-Laserpuls, dessen Querschnitt mit einem angepassten räumlichen Intensitätsprofil moduliert war, erzeugt. Beleuchten eines Halbleiters erzeugt eine Brechungsindex-Landschaft, dessen Beschaffenheit auf einer $4\text{ }\mu\text{m} \times 4\text{ }\mu\text{m}$ großen Fläche, durch einen räumlichen Lichtmodulator (SLM) definiert werden kann. Amplitude und Phase der Transmission der photo-induzierten Metamaterialien wurden mit Terahertz-Zeitdomänen-Spektroskopie von 0.5 bis 2.5 THz gemessen. In der Entstehung des experimentellen Aufbaus, wurde der räumliche Lichtmodulator installiert und charakterisiert. Eine Intensitäts-Modulationstiefe von über 99% wurde erreicht, wodurch die Erzeugung von Intensitätsprofilen mit hohem Kontrast garantiert werden kann. Vermessen der Punktspreizfunktion und Berechnung einer zweidimensionalen Kreuzkorrelation versicherten präzise Abbildungen.

Zeitaufgelöste Zeitdomänen-Spektroskopie der unangeregten Halbleiter wurde genutzt, um die optischen Konstanten der transienten Strukturen, ihr Fluenzverhalten und dessen Dynamik zu bestimmen. Das gemessene komplexwertige Transmissionspektrum wurde mit einer Kombination von Drude Modell, Fresnelschen Formeln und effektiver Mediums Theorie modelliert.

Um den Aufbau zu testen, wurden Drahtgitter-Polarisatoren, Dipolantennen und Ringe erzeugt. Die transienten Drahtgitter-Polarisatoren erreichten ein Auslöschungsverhältnis von ca. 10. Mit Hilfe dieser Strukturen, wurde zudem der Gültigkeitsbereich des Babinetischen Prinzips untersucht. Es zeigte sich, dass das Babinetische Prinzip mit zunehmend metallischen Strukturen besser erfüllt war. Gallium Arsenid und Silizium (welche eine Eindringtiefe von ≈ 1 und $10\text{ }\mu\text{m}$ besitzen) zeigen vergleichbare Ergebnisse.

Die Dipolantennen zeigten ein breitbandiges Hochpass Filterverhalten, wohingegen die rechteckigen Ring-Metamaterialien eine engbandige Resonanz zeigten, welche möglicherweise von lokal verstärkten Feldern begleitet wird. Beide Strukturen ermöglichen Auslöschungsverhältnisse von ca. 6.

In zukünftigen Untersuchungen erlauben transiente Metamaterialien das Erzeugen von schaltbaren Filtern, welche innerhalb von $\approx 100\text{ fs}$ eine Modulation von Terahertz Pulsen in einem Halbleiter ermöglichen.

A. Appendix

A.1. SLM phase shift calibration - Contrast

A Spatial Light Modulator (SLM) is a pixelated liquid crystal display in which the birefringence of each pixel can be computer-controlled individually. For each pixel the SLM converts an electric input into an optical phase shift via reorientation of liquid crystals. While this digital nature enables a small sized and cost effective driver unit, it introduces phase instabilities compared to analogue addressing. This phase flicker originates from the limited viscosity of liquid crystal molecules and can be troublesome for some applications and should be reduced. Each single addressing pulse has to be followed at a fraction depending on LC viscosity and frequency of the voltage change, in which higher addressing frequencies result in weaker flicker. A shorter pulse sequence creates less distinguishable phase levels with lower flicker compared to a longer sequence. The current configuration has 192 discrete voltage levels available to drive the SLM. Thus 256 (8 bit) input values have to map 192 voltages in a linear relation between input and applied phase delay. If a only fraction of the maximum photo-excitation is needed, a linear relationship allows easier rescaling.

The relation between the SLM input and the output optical phase shift has to be determined. Vaughan [Vau05] proposed the following method. A polarizer is placed in front of the SLM at a 45° towards the ordinary axis of the liquid crystal. The SLM is birefringent and a phase shift is applied to only one polarization axis of the incoming beam. The polarization will thus change as a function of the input voltage. By passing the beam through the polarizer again, the amplitude is modulated, which can be monitored with a camera (cf A.1a). Averaging the light intensity of each picture and scanning through all input values yields the desired relation between pixel brightness (phase shift) and intensity. The summed intensity on the CCD as a function of the SLM input is given in fig. A.1(b). The intensity modulation depth exceeds 99% and therefore guarantees precise photo-excitation.

The initial rise of the intensity for low pixel brightness is not yet (see also [Spr08]). The rise in intensity is probably caused by an inherent birefringence of the SLM. The parallel polarization will then always be given a phase delay compared to the orthogonal polarisation. Initially, an applied phase delay will compensate this inherent refractive index difference and cause the intensity to rise.

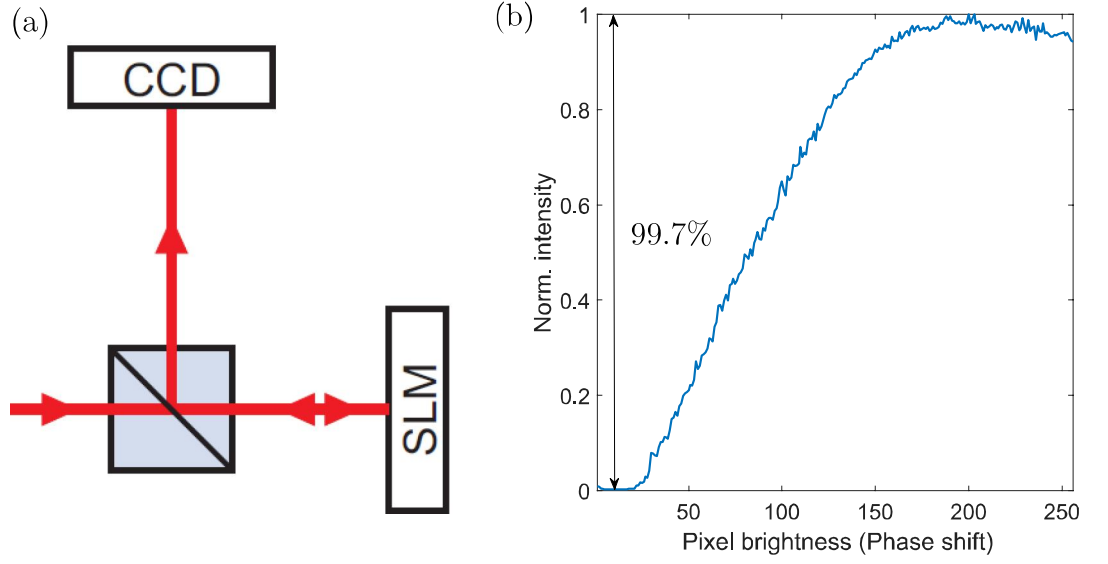


Figure A.1.: (a) Vaughan calibration setup using a polarizing beamsplitter to convert phase modulation into amplitude modulation. (b) Measured intensity on a CCD for varying phase delays 45° as in (a). The SLM input is defined by the brightness of the pixels sent to the SLM.

A.2. Fresnel transmission formulae

By traveling through a medium of complex refractive index $\tilde{n} = n + i\kappa$ a wave acquires a phase proportional to both the thickness d and n , while the amplitude decreases exponentially with κ . At any discontinuity of the refractive index the wave is partially transmitted and reflected. Multiple interfaces lead to interfering reflections resulting in non-trivial complex valued transmission spectra. The transfer matrix method, an approach based on the Fresnel formula, can be utilized for sample characterization. In this thesis a simplified version neglecting reflections, which appear not within the probed time-domain, is used. By fitting the calculated transmission to the experiment the dielectric properties of a single layer can be extracted.

A continuous plane-wave in a medium A with a refractive index $\tilde{n}_A = n_A + i\kappa_A$ traveling along the x -axis, with angular frequency ω and wavenumber $k_A = \tilde{n}_A \omega/c$, is described as

$$E_A^\pm(x, t) = E_A^\pm e^{i(\pm k_A x - \omega t)}. \quad (\text{A.1})$$

At an interface between media A and B , the amplitude Fresnel coefficients for reflection and transmission can be derived from Maxwell's equations:

$$r_{AB} = \frac{\tilde{n}_B - \tilde{n}_A}{\tilde{n}_B + \tilde{n}_A}, \quad (\text{A.2})$$

$$t_{AB} = \frac{2\tilde{n}_A}{\tilde{n}_B + \tilde{n}_A}. \quad (\text{A.3})$$

All waves inside the stack can be described as a sum of transmission and reflection using $r_{AB} = -r_{BA}$ and $r_{AB}^2 + t_{AB}^2 = 1$. While propagation through a layer the waves experience an increase in phase and a reduction of the amplitude according to

$$P_B(d) = e^{k_B d i}, \quad (\text{A.4})$$

where d is the thickness of the layer. The real part of k contributes to the phase, while the imaginary part describes the losses due to absorption.

The propagation through a series of layers can now be described by multiplication of the relevant Fresnel and propagation coefficients. Figure ?? depicts the schematic transmission of the THz wave through the sample. In the case of pumped semiconductors at least two layers have to be considered. Within in the absorption length d_{Abs} of the sample, one can assume a homogeneously pumped layer, while the rest of the sample remains unexcited. While multiple reflections within the unpumped layer can be neglected due to the long optical path length, they have to be considered within the excited layer. Using the geometrical row, the multiple reflection can considered through

$$M_{BC} = 1 + r_{BC} r_{BA} P_B^2. \quad (\text{A.5})$$

A. Appendix

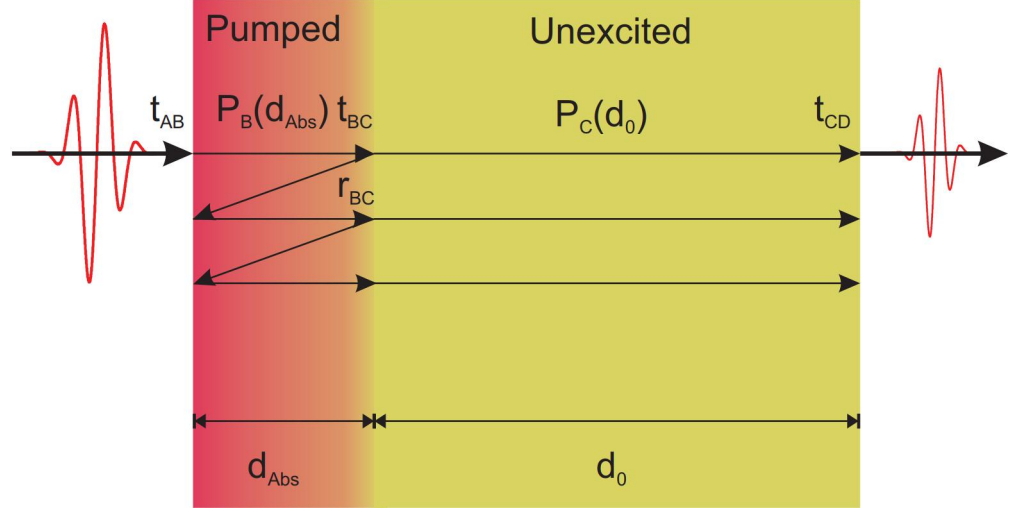


Figure A.2.: Heatmap of calculated absorbed energy density $W(u, z)$ of a homogeneous pump pulse for (a) $375 \mu\text{m}$, reduced to $60 \mu\text{m}$, and (b) $5 \mu\text{m}$ Silicon sample. In case of the thick sample pure Lambert-Beer-type absorption occurs, while additional interferences of the forward-propagating and reflected pump pulse at the end of the thin sample can be observed.

Assuming the only one incident wave and considering reflection only for the excited layer, the total transmission of d thick layer, can be described by the transmission function

$$T_{AD} = t_{AB} P_B(d_{\text{Abs}}) t_{BC} P_C(d - d_{\text{Abs}}) t_{CD} / M_{BC}. \quad (\text{A.6})$$

This complex transmission coefficient can be obtained experimentally via THz-TDS, as explained in chapter 4.1. Fitting the total transmission coefficient to the experimental data enables extraction of the complex refractive index \tilde{n} of the sample.

A.3. Pump-pulse absorption pattern

The shadow mask (at $z = -2f$) has a periodic spatial structure and so diffracts the pump beam into several discrete directions. An achromatic doublet pair (at $z = -1f$) collects and refocuses the diffracted waves onto the Si slab surface (at $z = 0$). To calculate the density $N(x, y, z)$ of the pump-induced electron-hole in the Si, we sum up all diffraction orders of the (scalar) pump electric field,

$$E(u, z, \omega) = \sum_{k_u} A(k_u) \exp(ik_u u) \left[e^{ik_z z} + r e^{ik_z (2d-z)} \right]. \quad (\text{A.7})$$

Here, u is the in-plane coordinate perpendicular (\perp) to the orientation of the wires, and z is the coordinate perpendicular to the Si slab. (The axis perpendicular to z and u is ignored because of translation-invariance along this direction.) Furthermore, $\omega/2\pi$ is a frequency of the pump pulse spectrum, and $A(k_u)$ is the amplitude of each Fourier component with wave vector k_u arising from diffraction by the shadow mask, as specified by Equation (A.8). Finally, the two terms in the square bracket describe the forward- and backward-propagating wave inside the Si slab, respectively, where r is the Fresnel reflection coefficient of the Si-air interface, and k_z is $(\omega^2 n^2 / c^2 - k_x^2)^{1/2}$. The amplitude of each diffracted wave is given by

$$A(k_u) = E_{inc}(\omega) \cdot \mathcal{F}[T(u)](k_u) \cdot F(k_u) \cdot t(k_u) \quad (\text{A.8})$$

where $E_{inc}(\omega)$ is the amplitude spectrum of the plane wave normally incident onto the shadow mask, and $T(u)$ is the spatial transmission function of our mask (square-wave-type, assuming values of 0 or 1 for dark and bright regions), and \mathcal{F} denotes a FT. Since T is periodic with period length a , only wave vectors $k_u = m2\pi/a$ come into play, where the integer m is the order of each diffracted wave. For the square-wave-type T of our mask, we have $\mathcal{F}[E_{inc}(\omega)T(u)](k_u) \propto \text{sinc}(\pi mb/a)$ where $\text{sinc}x = \sin x/x$, and $b - a$ is the width of each shadowing stripe of the mask; The filter function F quantifies the finite aperture size of the lens, and in our setup, F is 1 for $|m| \leq 3$ and 0 otherwise. Finally, $t(k_u)$ is the Fresnel transmission coefficient of the air-Si interface.

We are primarily interested in the pump-induced electron-hole density $N(u, z)$ which is proportional to the locally absorbed power $W(u, z)$ of the pump pulse, that is,

$$W(u, z) \propto \int dt E^2(u, z, t) \propto \int d\omega |E(u, z, \omega)|^2 \quad (\text{A.9})$$

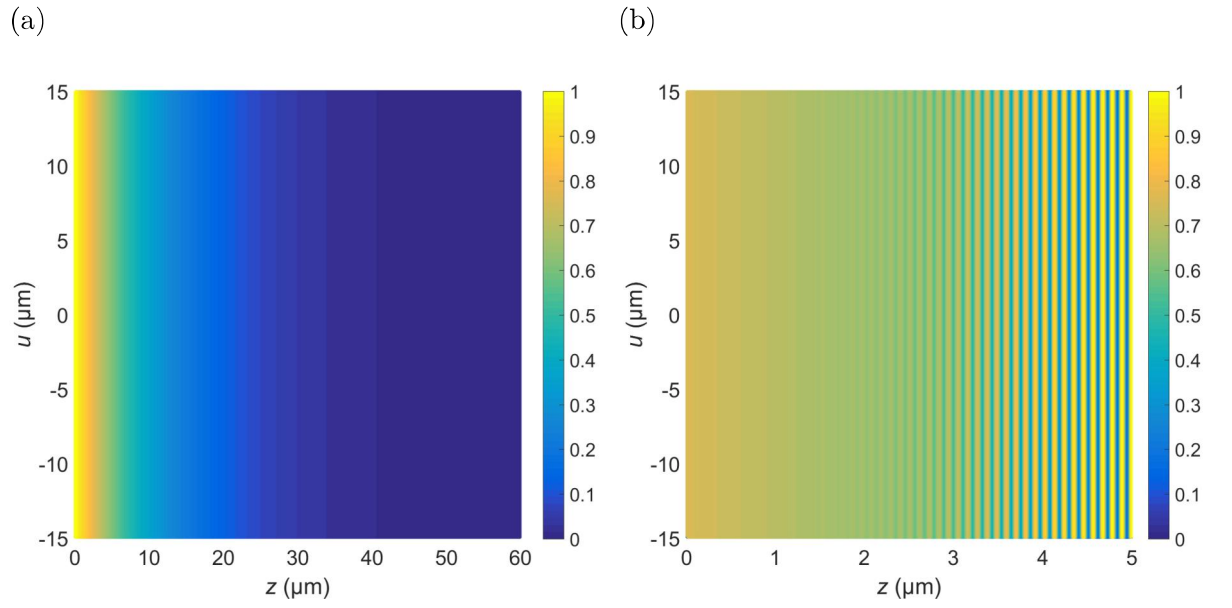


Figure A.3.: Heatmap of calculated absorbed energy density $W(u, z)$ of a homogeneous pump pulse for (a) 375 μm , reduced to 60 μm , and (b) 5 μm Silicon sample. In case of the thick sample pure Lambert-Beer-type absorption occurs, while additional interferences of the forward-propagating and reflected pump pulse at the end of the thin sample can be observed.

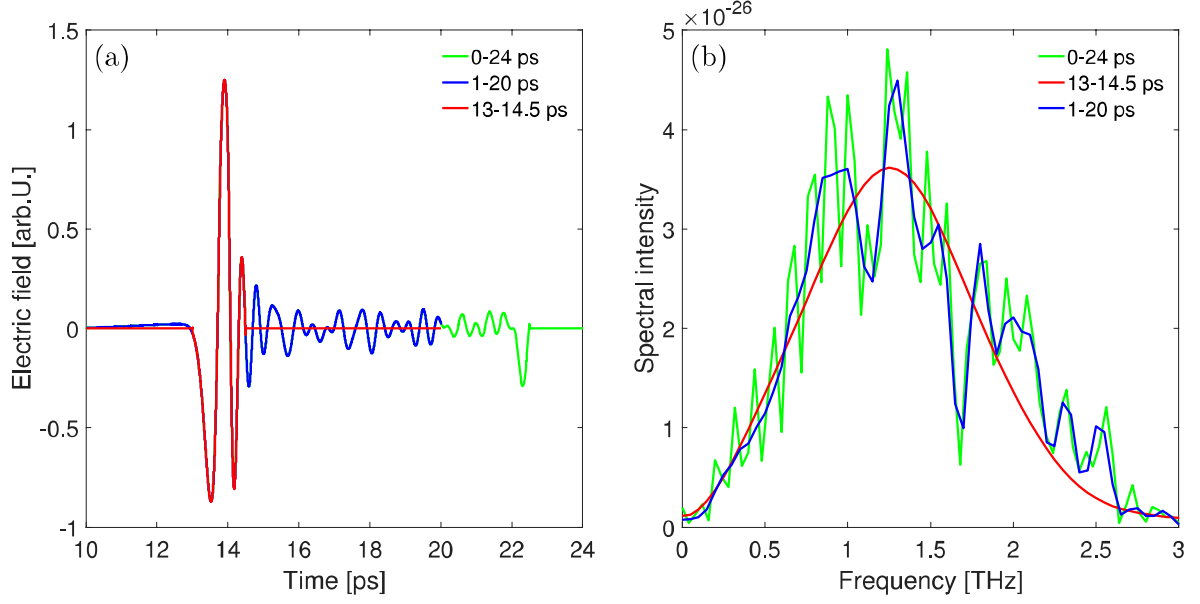


Figure A.4.: Effect of various rectangular window function sizes on the characteristic time domain transients of the experimental setup without specimen. The corresponding intensity spectra are shown in (b). Narrow windows (red curve) increase the signal-to-noise ratio whilst smoothing the spectra. Wide window functions (green) maintain the shape of the spectra while offering a worse signal-to-noise ratio. A balanced window size (blue) enable shape preservation and sufficient signal-to-noise.

A.4. Windowing effects on Fourier transformation

Terahertz time domain spectroscopy allows the direct extraction of the optical properties of the sample, e.g. complex refractive index. This technique relies on electro-optic sampling, which enables the direct detection of the full time domain signal, acquiring amplitude and phase information simultaneously. The complex spectrum of this THz pulse can be acquired by Fourier transforming the transient according to

$$\tilde{E}(\nu) \equiv F\{E(t)\} = \int E(t)e^{i2\pi\nu t} dt. \quad (\text{A.10})$$

One of the limitations of using the Fourier transform to construct an spectrum, is the assumption of an infinitely periodic input signal in the time domain, while only a margin of the time-domain is accessible for evaluation. Furthermore the sample and optical components induce reflections, certain resonances, i.e. water on the sample or perturbations on the electro-optic signal, affecting the shape of the electric field. Therefore the signal has to be divided into useful information and noise. For filtering, the signal is multiplied with window function in the time domain. A typical THz field transient measured in this configuration under varying rectangular window functions is shown in figure A.4(a). However imprudent use of window functions can lead to truncation artifacts and line resolution issues. To mitigate this issue, zeros are appended to the end of the time-domain signal before the Fourier transform is performed in a process called zero-padding. While this process does not alter the information in the spectrum nor does it improve its resolution, it improves the resolution of the FT and hence also improves the appearance of the spectrum and visibility of the

A. Appendix

peaks. To allow for direct comparability in the frequency domain all signals are interpolated with a piecewise cubic hermite interpolating polynomial over the same time-window.

The intensity spectra are the result of both the characteristic response of the experimental setup and the used window function. The spectrum of the transmitted intensity, which is the absolute square of equation A.10, is shown in figure A.4(b). As can be seen in regard to the red curve, narrow windows lead to a smoothed spectra resulting in a loss of information, i.e the water resonance at roughly 1.65 THz vanishes. In the counterpart wide windows (green) gather up perturbations, e.g. reflections of the original signal, which are not part of the relevant signal, falsifying the spectra. Hence a balanced window size (blue) has to be utilized to guarantee high signal-to-noise ratios and no foreign content in the signal while maintaining the overall shape of the spectrum.

A.5. 2D cross correlation - global image quality

The point-spread-function determines the local image quality, which is crucial for modulation depth of metamaterials. But while, the single unit cell of a metamaterial induces certain modulations, the overall response depends on averaged/effective response of the whole material. On this account the global image quality has to be warranted.

Comparing the similarity of two signals is an essential task and a numeric measure of similarity is (cross-)correlation, which is similar two the convolution of two functions. When comparing images, the cross-correlation becomes a sum of pairwise multiplications of corresponding pixel values of the images.

Though this method reflects the similarity of the images being compared, it is error-prone. Especially different image sources, distinctions in terms of brightness falsify the results. However normalizing the cross-correlation for each image allows more robust measurement of image similarity. The formula for the normalized cross-correlation is

$$\text{NCC}(\text{Image1}, \text{Image2}) = \frac{1}{N\sigma_1\sigma_2} \sum_{x,y} \left(\text{Image1}(x,y) - \overline{\text{Image1}} \right) \times \left(\text{Image2}(x,y) - \overline{\text{Image2}} \right), \quad (\text{A.11})$$

where N is the number of pixels and $\sigma_{1/2}$ is the standard deviation of Image1/2. The result of the NCC is scaled to $[-1, 1]$. Identical images yield 1, while an image and its negation equals -1. With this normalized cross-correlation it's possible to determine the parts of an image that match a predefined template regardless of their orientation and local brightness. To identify positions that match the template correlation, their correlation values have to be higher than a predefined threshold value (i.e. stronger than 0.9) and locally maximal.

In this thesis the 2D cross-correlation compares a template, e.g. a single unit cell, with the whole image. In figure A.5 a recorded CCD image is shown, while the matched template is shown in the inset. The red dots on the image represent the cross-correlation points with sufficient accordance. The majority of unit cells satisfies the quality conditions, confirming the projection setup. Still some unit cells are overlapped with diffraction patterns, which are induced by particles and dirt on a neutral density filter positioned in front of the camera to prevent camera saturation due to high intensities. Additionally damaged SLM pixels can be spotted over the inset, impeding all modulation of connected row and column pixels. While the particles, dust and dirt on the neutral density filter are negligible for the experiment, the damaged SLM pixels disturb the homogeneity of the metamaterials and therefore an undamaged area has to be used for high quality transient modulation.

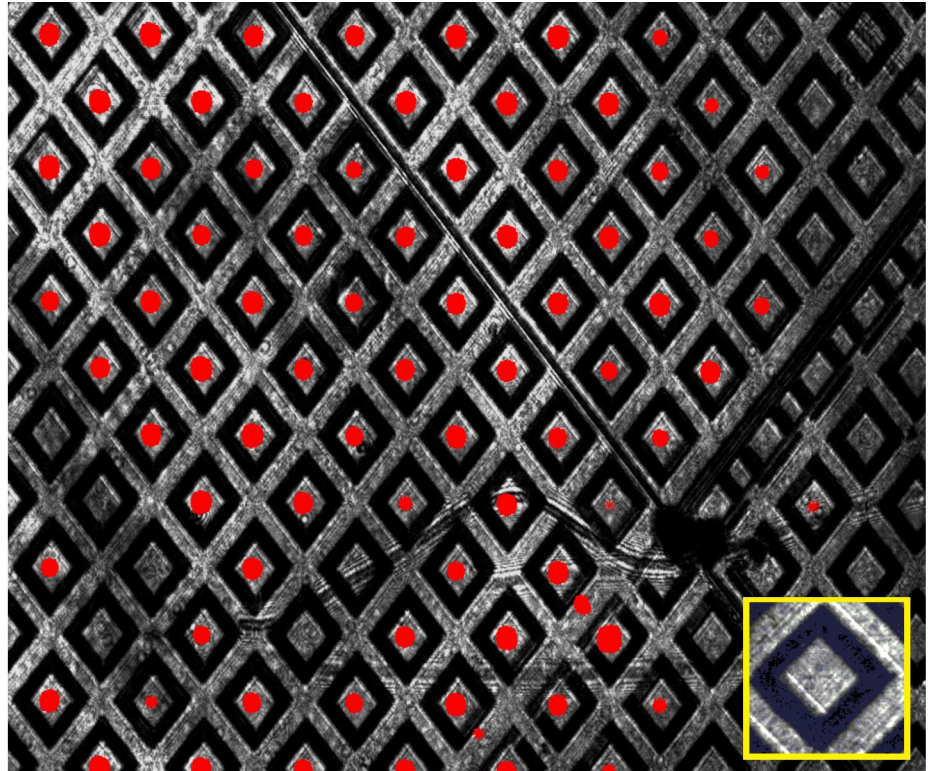


Figure A.5.: Recorded intensity pattern on a CCD camera behind a neutral density filter. The 2D cross-correlation is calculated with the template in the inset. Correlation points with a value greater than 0.8 are marked with a red dot, proving the overall image quality. While the majority of unit cell fulfills the quality conditions some pixels are superimposed with diffraction patterns of dirt and dust on the neutral density filter or damaged pixel on the SLM, which prevent modulation.

Bibliography

- [Ash76] N. Ashcroft & N. Mermin. *Solid State Physics*. Holt-Saunders, 1976.
- [Aus83] D. H. Auston. *Generation and detection of millimeter waves by picosecond photoconductivity*. Applied Physics Letters **43**, 7, (1983) 631.
- [Bab37] J. Babinet. *Memoires d’optique meteorologique*. 1837.
- [Bin08] C. M. Bingham, H. Tao, X. Liu, D. Abbott, X. Zhang, & W. J. Padilla. *Planar wallpaper group metamaterials for novel terahertz applications*. Optics Express **16**, 23.
- [Boo46] H. Booker. *Slot aerials and their relation to complementary wire aerials (Babinet’s principle)* (1946).
- [Bor70] M. Born & E. Wolf. *Principles of Optics*. 1970.
- [Bur16] L. Burger. *Novel implementation of a phase-only spatial light modulator for laser beam shaping*. Dissertation, National Metrology Institute of South Africa (2016).
- [Bus12] S. Busch, B. Scherger, M. Scheller, & M. Koch. *Optically controlled terahertz beam steering and imaging*. Optics Letters **37**, 8.
- [Cai10] W. Cai & V. Shalaev. *Optical Metamaterials Fundamentals and Applications*. Springer, 2010.
- [Can81] J. A. Cantor, P. K. Cheo, M. C. Foster, & L. A. Newman. *Application of Submillimeter Wave Lasers to High Voltage Cable Inspection*. IEEE JOURNAL OF QUANTUM ELECTRONICS **17**, 4.
- [Che06] H. T. Chen, W. J. Padilla, J. M. Zide, A. C. Gossard, A. J. Taylor, & R. D. Averitt. *Active terahertz metamaterial devices*. Nature **444**, 7119, (2006) 597.
- [Che08a] H. T. Chen, H. Lu, A. K. Azad, R. D. Averitt, A. C. Gossard, S. a. Trugman, J. F. O’Hara, & A. J. Taylor. *Electronic control of extraordinary terahertz transmission through subwavelength metal hole arrays*. Optics Expres **16**, 7641.
- [Che08b] H.-T. Chen, J. F. O’Hara, A. K. Azad, A. J. Taylor, R. D. Averitt, D. B. Shrekenhamer, & W. J. Padilla. *Experimental demonstration of frequency-agile terahertz metamaterials*. Nature Photonics **2**, 5, (2008) 295.
- [Che09] H.-T. Chen, W. J. Padilla, M. J. Cich, A. K. Azad, R. D. Averitt, & A. J. Taylor. *A metamaterial solid-state terahertz phase modulator*. Nature Photonics **3**, 3, (2009) 148.

Bibliography

- [dA11] J. A. del Alamo. *Nanometre-scale electronics with III-V compound semiconductors*. Nature **479**, 7373, (2011) 317.
- [Did07] S. A. Diddams, L. Hollberg, & V. Mbele. *Molecular fingerprinting with the resolved modes of a femtosecond laser frequency comb*. Nature **445**, 7128, (2007) 627.
- [Fed10] J. Federici & L. Moeller. *Review of terahertz and subterahertz wireless communications*. Journal of Applied Physics **107**, 11, (2010) 111101.
- [Feu03] T. Feurer, J. C. Vaughan, & K. A. Nelson. *Spatiotemporal Coherent Control of Lattice Vibrational Waves*. Science **299**.
- [Fle74] J. Fleming. *High-Resolution Submillimeter-Wave Fourier-Transform Spectrometry of Gases*. IEEE TRANSACTIONS ON MICROWAVE THEORY AND TECHNIQUES **22**, 12.
- [Geo14] G. Georgiou, H. K. Tyagi, P. Mulder, G. J. Bauhuis, J. J. Schermer, & J. G. Rivas. *Photo-generated THz antennas*. Sci Rep **4**, (2014) 3584.
- [Gil04] I. Gil, J. Garcia-Garcia, J. Bonache, F. Martin, M. Sorolla, & R. Marques. *Varactor-loaded split ring resonators for tunable notch filters at microwave frequencies*. Electronics Letters **40**, 21, (2004) 1347.
- [Hau08] J. Hau, A. Lakhtakia, & C. Qiu. *Terahertz metamaterials with semiconductor split-ring resonators for magnetostatic tunability*. Optics Express **16**, 19.
- [Hil11] D. Hillerkuss, R. Schmogrow, T. Schellinger, M. Jordan, M. Winter, G. Huber, T. Valaitis, R. Bonk, P. Kleinow, F. Frey, M. Roeger, S. Koenig, A. Ludwig, A. Marculescu, J. Li, M. Hoh, M. Dreschmann, J. Meyer, S. Ben Ezra, N. Narkiss, B. Nebendahl, F. Parmigiani, P. Petropoulos, B. Resan, A. Oehler, K. Weingarten, T. Ellermeyer, J. Lutz, M. Moeller, M. Huebner, J. Becker, C. Koos, W. Freude, & J. Leuthold. *26 Tbit/s line-rate super-channel transmission utilizing all-optical fast Fourier transform processing*. Nature Photonics **5**, 6, (2011) 364.
- [Jia03] Z. Jian, J. Pearce, & D. M. Mittleman. *Characterizing individual scattering events by measuring the amplitude and phase of the electric field diffusing through a random medium*. Phys Rev Lett **91**, 3, (2003) 033903.
- [Kac06] J. Kacperski & M. Kujanwinska. *Active, LCoS based laser interferometer for microelements studies*. Optics Express **14**, 21.
- [Kam10] T. Kampfrath, A. Sell, G. Klatt, A. Pashkin, S. Mährlein, T. Dekorsy, M. Wolf, M. Fiebig, A. Leitenstorfer, & R. Huber. *Coherent terahertz control of antiferromagnetic spin waves*. Nature Photonics **5**, 1, (2010) 31.
- [Kam13] T. Kampfrath, K. Tanaka, & K. A. Nelson. *Resonant and nonresonant control over matter and light by intense terahertz transients*. Nature Photonics **7**, 9, (2013) 680.

- [Kam14] N. Kamaraju, A. Rubano, L. Jian, S. Saha, T. Venkatesan, J. Nötzold, R. Kramer Campen, M. Wolf, & T. Kampfrath. *Subcycle control of terahertz waveform polarization using all-optically induced transient metamaterials*. Light: Science & Applications **3**, 2, (2014) e155.
- [Kaw03] K. Kawase, Y. Ogawa, & Y. Watanabe. *Non-destructive terahertz imaging of illicit drugs using spectral fingerprints*. Optics Express **11**, 20.
- [Kem92] M. Kempe, U. Stamm, B. Wilhelmi, & W. Rudolph. *Spatial and temporal transformation of femtosecond laser pulses by lenses and lens systems*. Optical Society of America .
- [Kem93] M. Kempe & W. Rudolph. *Impact of chromatic and spherical aberration on the focusing of ultrashort light pulses by lenses*. Optics letters **18**, 2.
- [Lcc15] D. K. Lcc, J. H. Kang, J. S. Lcc, H. S. Kim, C. Kim, J. H. Kim, T. Lcc, J. H. Son, Q. H. Park, & M. Seo. *Highly sensitive and selective sugar detection by terahertz nano-antennas*. Sci Rep **5**, (2015) 15459.
- [Lei08] S. Leinb, T. Kampfrath, K. Volkmann, M. Wolf, J. T. Steiner, M. Kira, S. W. Koch, A. Leitenstorfer, & R. Huber. *Terahertz coherent control of optically dark paraexcitons in Cu₂O*. Phys Rev Lett **101**, 24, (2008) 246401.
- [Lew06] C. Lewis, M. C. Kemp, & G. P. Owen. *Millimetre wave and terahertz technology for the detection of concealed threats: a review* **6402**, (2006) 64020D.
- [Lia15] Y. Liang. *Nematic Liquid Crystal* (2015).
- [Mau04] J. Maultzsch, S. Reich, C. Thomsen, H. Requardt, & P. Ordejón. *Phonon dispersion of graphite*. Physical Review Letter **92**, 7.
- [Mos05] H. O. Moser, B. D. F. Casse, O. Wilhelmi, & B. T. Saw. *Terahertz Response of a Microfabricated Rod-Split-Ring-Resonator Electromagnetic Metamaterial*. Physical Review Letters **94**, 6.
- [Mä16] S. Mährlein. *Nonlinear Terahertz Phononics: A Novel Route to Controlling Matter*. Dissertation, Freie Universität Berlin (2016).
- [Naf07] M. Naftaly & R. E. Miles. *Terahertz Time-Domain Spectroscopy for Material Characterization*. Proceedings of the IEEE **95**, 8.
- [O'H07] J. F. O'Hara, E. Smirnova, H.-T. Chen, A. J. Taylor, R. D. Averitt, C. Highstrete, M. Lee, & A. J. Padilla. *Properties of Planar Electric Metamaterials for Novel TeraHertz Applications*. Journal of Nanoelectronics and Optoelectronics **2**, 1, (2007) 90.
- [Oka10] T. Okada, S. Tsuji, K. Tanaka, K. Hirao, & K. Tanaka. *Transmission properties of surface plasmon polaritons and localized resonance in semiconductor hole arrays*. Applied Physics Letters **97**, 26, (2010) 261111.
- [Oka11] T. Okada & K. Tanaka. *Photo-designed terahertz devices*. Sci Rep **1**, (2011) 121.

Bibliography

- [Par14] S. J. Park, J. T. Hong, S. J. Choi, H. S. Kim, W. K. Park, S. T. Han, J. Y. Park, S. Lee, D. S. Kim, & Y. H. Ahn. *Detection of microorganisms using terahertz metamaterials*. Sci Rep **4**, (2014) 4988.
- [Pei13] K.-E. Peiponen, J. Zeitler, & M. Kuwata-Gonokami. *Terahertz Spectroscopy and Imaging*. Springer, 2013.
- [Pen99] J. Pendry, A. J. Holden, D. Robbins, & W. Stewart. *Magnetism from Conductors and Enhanced Nonlinear Phenomena*. IEEE Transactions on Microwave Theory and Techniques **47**, 11.
- [Poc77] Y. Pochi, Y. Amnon, & C.-S. Hong. *Electromagnetic propagation in periodic stratified media. i. general theory*. Optical Society of America **67**, 4.
- [Poc78] Y. Pochi. *A new optical model for wire grid polarizers*. Optics Communications **26**, 3.
- [Poc81] Y. Pochi. *Generalized model for wire grid polarizers*. Proc. of SPIE, Polarizers and Applications **307**.
- [Pod08] A. Podzorov & G. Gallot. *Low-loss polymers for terahertz applications*. Applied Optics **47**, 18.
- [Pry10] I. M. Pryce, K. Aydin, Y. A. Kelaita, R. M. Briggs, & H. A. Atwater. *Highly strained compliant optical metamaterials with large frequency tunability*. Nano Lett **10**, 10, (2010) 4222.
- [RA15] M. Rosete-Aguilar, J. Garduno-Mejía, & N. C. Bruce. *Focusing ultrashort laser pulses with achromatic doublets*. SPIE .
- [Rei13] S. Reichelt. *Spatially resolved phase-response calibration of liquid-crystal-based spatial light modulators*. APPLIED OPTICS **52**, 12.
- [Riz13] C. Rizza, A. Ciattoni, L. Columbo, M. Brambilla, & F. Prati. *Terahertz optically tunable dielectric metamaterials without microfabrication*. Optics Letters **38**, 8, (2013) 1307.
- [Sax12] A. K. Saxena. *High-Temperature Superconductors*, Bd. 125. Springer, 2012.
- [Sch11] B. Scherger, M. Scheller, C. Jansen, M. Koch, & K. Wiesauer. *Terahertz lenses made by compression molding of micropowders*. Applied Optics **50**, 15.
- [Sch15] E. F. Schubert. *Doping in III-V semiconductors*. Schubert, E. Fred, 2015.
- [Sha99] J. Shah. *Ultrafast spectroscopy of semiconductors and semiconductor nanostructures*, Bd. 115. Springer Verlag, 1999.
- [Sie02] P. H. Siegel. *Terahertz Technology*. IEEE TRANSACTIONS ON MICROWAVE THEORY AND TECHNIQUES **50**, 3.
- [Sie04] P. H. Siegel. *Terahertz Technology in Biology and Medicine*. Microwave Symposium Digest, 2004 IEEE MTT-S International .

- [Sin11] R. Singh, A. K. Azad, Q. X. Jia, A. J. Taylor, & H.-T. Chen. *Thermal tunability in terahertz metamaterials fabricated on strontium titanate single-crystal substrates*. Optics Letters **36**, 7.
- [Smi88] P. R. Smith, D. H. Auston, & M. C. Nuss. *Subpicosecond Photoconducting Dipole Antennas*. IEEE JOURNAL OF QUANTUM ELECTRONICS **24**, 2.
- [Spe91] D. E. Spence, J. M. Evans, W. E. Sleat, & W. Sibbet. *Regeneratively initiated self-mode-locked Ti:sapphire laser*. Optics Letters **16**, 22.
- [Spr08] D. P. Sprünken. *A 2D Spatial Light Modulator for spatio-temporal shaping*. Dissertation, University of Twente (2008).
- [Tak14] Y. Takiguchi, T. Otsu, T. Inoue, & H. Toyoda. *Self-distortion compensation of spatial light modulator under temperature-varying conditions*. Opt Express **22**, 13, (2014) 16087.
- [Tao08] H. Tao, A. C. Strikwerda, K. Fan, C. M. Bingham, W. J. Padilla, X. Zhang, & R. D. Averitt. *Terahertz metamaterials on free-standing highly-flexible polyimide substrates*. Journal of Physics D: Applied Physics **41**, 23, (2008) 232004.
- [Tha13] C. Thacker, A. Cooray, J. Smidt, F. De Bernardis, K. Mitchell-Wynne, A. Amblard, R. Auld, M. Baes, D. L. Clements, A. Dariush, G. De Zotti, L. Dunne, S. Eales, R. Hopwood, C. Hoyos, E. Ibar, M. Jarvis, S. Maddox, M. J. Michałowski, E. Pascale, D. Scott, S. Serjeant, M. W. L. Smith, E. Valiante, & P. van der Werf. *H-Atlas: The Cosmic Abundance of Dust from the Far-Infrared Background Power Spectrum*. The Astrophysical Journal **768**, 1, (2013) 58.
- [Vau05] J. C. Vaughan. *Two-Dimensional Ultrafast Pulse Shaping and its Application to Coherent Control and Spectroscopy*. Dissertation, MASSACHUSETTS INSTITUTE OF TECHNOLOGY (2005).
- [vE89] M. van Exter, C. Fattinger, & D. Grischkowsky. *Terahertz time-domain spectroscopy of water vapor*. Optics Letters **14**, 20.
- [Xie13] Z. Xie, X. Wang, J. Ye, S. Feng, W. Sun, T. Akalin, & Y. Zhang. *Spatial Terahertz Modulator*. Scientific Reports **3**.
- [Yac03] B. G. Yacobi. *Semiconductor Materials An Introduction to Basic Principles*. Springer US, 2003.
- [Yam09] I. Yamada, K. Takano, M. Hangyo, M. Saito, & W. Watanabe. *Terahertz wire-grid polarizers with micrometer-pitch Al gratings*. Optics Letters **34**, 3.
- [Yen04] T. J. Yen, W. J. Padilla, N. Fang, D. C. Vier, D. R. Smith, J. Pendry, D. N. Basov, & X. Zhang. *Terahertz Magnetic Response from Artificial Materials*. Science **303**.
- [Yu12] N. Yu, F. Aieta, P. Genevet, M. A. Kats, Z. Gaburro, & F. Capasso. *A broadband, background-free quarter-wave plate based on plasmonic metasurfaces*. Nano Lett **12**, 12, (2012) 6328.

Bibliography

- [Zer65] F. Zernike & P. R. Berman. *Generation of Far Infrared as a Difference Frequency*. Physical Review Letters **15**, 26, (1965) 999.
- [Zha07] Q. Zhao, L. Kang, B. Du, B. Li, J. Zhou, H. Tang, X. Liang, & B. Zhang. *Electrically tunable negative permeability metamaterials based on nematic liquid crystals*. Applied Physics Letters **90**, 1, (2007) 011112.
- [Zhe16] N. I. Zheludev & E. Plum. *Reconfigurable nanomechanical photonic metamaterials*. Nat Nanotechnol **11**, 1, (2016) 16.
- [Zhu11] W. M. Zhu, A. Q. Liu, X. M. Zhang, D. P. Tsai, T. Bourouina, J. H. Teng, X. H. Zhang, H. C. Guo, H. Tanoto, T. Mei, G. Q. Lo, & D. L. Kwong. *Switchable magnetic metamaterials using micromachining processes*. Adv Mater **23**, 15, (2011) 1792.

Acknowledgment

I would like to thank everyone who took part in my scientific work. Especially I would like to mention the following supportive people:

The biggest thanks go to Tobias Kampfrath. He was the role model of a supervisor, who supported me with his knowledge and always encouraged me. Thank you.

I wish to thank Prof. Ulrike Woggon for being my first supervisor and inspired me with all her lectures.

I wish to thank Prof. Martin Wolf for being my secondary supervisor, and the great environment in the department of physical chemistry at the FHI.

With the scientific and moral support of my colleagues Mohsen Sajadi, Tom Seifert, Lukas Braun, Oliver Gückstock and Lukáš Nádvorník, this would have been impossible. Additionally, I would like to thank Sebastian Mährlein for every advice regarding the setup, writing, science and life itself. Furthermore I'd like to thank Julius Heitz, who was always listening to all of my issues and helped wherever he could.

Finally, I would like to thank my parents, Bernard and especially my brother, for their unconditional support.

Declaration of Authorship

I hereby certify that this thesis has been composed by me and is based on my own work, unless stated otherwise. No other person's work has been used without due acknowledgement in this thesis. All references and verbatim extracts have been quoted, and all sources of information, including graphs and data sets, have been specifically acknowledged.

Date:

Signature: